GERMAN - MONGOLIAN INSTITUTE FOR RESOURCES AND TECHNOLOGY

The present work was submitted to the Faculty of Mechanics and Electrical Engineering

Comparative Simulations of Thermal Management Strategies for EV $LiFePO_4$ Battery Modules in Mongolian Cold Climates

Bachelor Thesis

by

Bilguun Dagvasambuu

Study program: **Mechanical Engineering**

Student ID: **B2200119**

Supervisor 1/Examiner 1 **Odbileg Norovrinchen**

Supervisor 2/Examiner 2 **Kim Yong Suk**

Ulaanbaatar/Nalaikh, 2026

Table of Contents

Table of Contents 1

Acknowledgement 3

List of Figures 4

List of Tables 5

List of Abbreviations 6

Abstract 7

1. Introduction 9

1.1 Background and Motivation 9

1.2 Problem Statement 11

1.3 Research Objectives 11

1.4 Scope and Limitations 12

1.5 Thesis Structure 13

2. State of the Art 14

2.1 $LiFePO_4$ Battery Technology 14

2.2 Effects of Low Temperature on Lithium-Ion Batteries 15

2.2.1 Performance Degradation at Low Temperatures 15

2.2.2 Aging Mechanisms at Low Temperatures 17

2.3 Thermal Management Strategies for EV Batteries 18

2.3.1 Passive Insulation with Aerogel (System A) 18

2.3.2 External PTC Resistive Heating (System B) 19

2.3.3 Internal AC Self-Heating (System C) 20

2.3.4 Phase Change Materials (System D) 21

2.4 Mongolian Climate Context 22

2.5 Summary and Research Gap 23

3. Materials and Methods 24

3.1 Battery Cell and Module Specifications 24

3.2 CAD Geometry Development 27

3.3 ANSYS Finite Element Analysis Setup 29

3.3.1 Geometry Import and Meshing 30

3.3.2 Material Properties 31

3.3.3 Thermal Management Systems Modelled 33
3.3.4 Boundary Conditions and Evaluation Metrics 36
4. Results **41**
4.1 System A: Aerogel Insulation 41
4.2 System B: External PTC Resistive Heating 43
4.3 System C: Internal AC Self-Heating 45
4.4 System D: Phase Change Material Buffer 46
4.5 System E: Combined Systems and Optimisation 49
4.5.1 Cold-Start Sub-Simulations E1 to E4 49
4.5.2 Summer Overheating Sub-Simulation E5 52
4.6 Comparative Summary and Efficiency Ranking 54
5. Discussion and Conclusions **56**
5.1 Discussion 56
5.1.1 Effectiveness of Each Strategy 56
5.1.2 Energy and Practical Considerations 58
5.1.3 Limitations of the Study 59
5.2 Conclusions 60
5.3 Recommendations for Future Work 61
6. References **63**
7. Statutory Declaration **65**

Acknowledgement

I would like to express my sincere gratitude to my thesis supervisors, Mr. Odbileg Norovrinchen and Mr. Yong Suk Kim, for their invaluable guidance, continuous encouragement, and unwavering support throughout the course of this research. Their insightful advice, patience, and dedication to academic excellence have been instrumental in the successful completion of my bachelor's thesis.

List of Figures

Figure 1: Seasonal mean temperature map of Mongolia

Figure 2: Discharge capacity as a function of temperature for LFP cells

Figure 3: 12S1P battery module assembly showing all twelve stacked cell bodies and terminal blocks, baseline geometry

Figure 4: CAD assembly model of the battery module with thermal management components

Figure 5: Finite element mesh of the battery module and heater plate (System B)

Figure 6: Minimum cell temperature versus time for System A and the Baseline

Figure 7: Temperature distribution across the aerogel-insulated module at t = 1,800 s

Figure 8: Temperature distribution across the module at the end of the System B simulation at t = 14,400 s

Figure 9: Temperature distribution at the moment the minimum cell temperature reaches 0°C in System C at t = 5,680 s

Figure 10: Temperature distribution across the module and PCM slab at t = 1,800 s (System D)

Figure 11: Minimum cell temperature versus time for System D and the Baseline

Figure 12: Minimum cell temperature versus time for System E sub-simulations E1 to E4

Figure 13: Temperature distribution in System E5 at the moment the maximum cell temperature reaches 60°C at t = 4,680 s

List of Tables

Table 1: CATL 100 Ah LFP prismatic cell specifications and thermal properties used in ANSYS

Table 2: Battery module configuration parameters

Table 3: Material properties assigned in ANSYS Engineering Data

Table 4: System E sub-simulation configurations

Table 5: Boundary conditions applied to all six simulation systems

Table 6: Analysis settings applied to all six Transient Thermal systems

Table 7: Heat retention test results for the Baseline and System A

Table 8: Heat retention test results for System D (PCM slab) versus the Baseline

Table 9: System E cold-start sub-simulation results

Table 10: Comparative performance summary of all thermal management strategies

Table 11: Efficiency ranking of active heating systems

List of Abbreviations

Abbreviation	Full Form
AC	Alternating Current
ANSYS	Analysis System (finite element analysis software)
BMS	Battery Management System
CAD	Computer-Aided Design
CATL	Contemporary Amperex Technology Co. Limited
DC	Direct Current
EV	Electric Vehicle
FEA	Finite Element Analysis
GMIT	German-Mongolian Institute for Resources and Technology
HEV	Hybrid Electric Vehicle
LFP	Lithium Iron Phosphate ($LiFePO_4$)
NCA	Nickel Cobalt Aluminium (lithium-ion chemistry)
NMC	Nickel Manganese Cobalt (lithium-ion chemistry)
PCM	Phase Change Material
PTC	Positive Temperature Coefficient
RMS	Root Mean Square
SEI	Solid Electrolyte Interphase
SOC	State of Charge
STEP	Standard for the Exchange of Product Data
TIM	Thermal Interface Material
TMS	Thermal Management System

Abstract

Mongolia ranks among the world's coldest inhabited nations, with Ulaanbaatar averaging −25°C in January and the national record reaching −58°C. These conditions severely impair the performance of lithium iron phosphate (LFP) battery modules: at −40°C, available power may be reduced by up to 80% relative to room-temperature performance, and charging is not safely possible without prior thermal conditioning due to the risk of permanent lithium plating at the graphite anode. Standard battery qualification tests are oriented to major markets in the United States, China, and Europe and are typically conducted only down to −25°C, leaving the extreme cold end of the Mongolian operational range uncharacterised in the published literature.

This thesis presents a comparative transient thermal finite element analysis of four individual thermal management strategies applied to a 12-series 1-parallel (12S1P) module of twelve CATL 100 Ah prismatic LFP cells, together with a fifth combined and optimisation system (System E) that evaluates five sub-simulations pairing active and passive strategies under cold-start and summer overheating conditions. The four individual strategies are: (A) passive aerogel insulation (thermal conductivity k = 0.016 W/(m·K), 7.5 mm thick); (B) external positive temperature coefficient (PTC) resistive heating at 150 W applied through a 404.14 mm × 200.33 mm × 10 mm heater plate; (C) internal alternating-current (AC) self-heating, modelled as a volumetric heat generation rate of 54,538 W/m^3 applied uniformly to all twelve cell bodies; and (D) a passive RT35 phase change material (PCM) buffer, modelled as a 404.14 mm × 200.33 mm × 3 mm slab on the module face opposite the heater plate.

Three-dimensional geometry was developed in Autodesk Inventor Professional 2026 and imported into ANSYS Workbench 2025 R2 for transient thermal analysis. Six Transient Thermal systems are defined: a Baseline representing the unprotected module, and Systems A through E. Two test types are used: heat retention tests (module starts at +20°C, cools in −40°C ambient) and heat-up tests (module starts at −40°C, warmed by active heat sources). Key results are as follows. System A (aerogel alone) extended the time before the minimum cell temperature crossed 0°C from 100 s (Baseline) to 3,140 s, a 31-fold improvement providing approximately 50 minutes of additional passive protection. System B (PTC heater alone) failed to bring any cell to 0°C within 4 hours; the minimum temperature after 14,400 s was −14°C. System C (AC self-heating alone) achieved 0°C minimum in 5,680 s. System D (PCM alone) extended minimum temperature protection by only 105 s, confirming aerogel outperforms PCM by a factor of 29 as a passive cold-weather strategy. System E identified the

combination of AC self-heating with aerogel insulation (E2) as optimal: 0°C minimum reached in 2,200 s (36.7 minutes) consuming only 0.458 kWh, the best efficiency of all active strategies tested. Adding PCM to active cold-start systems was found to be detrimental, extending warm-up time in both E3 and E4 by absorbing heat that would otherwise warm the cells. System E5, a summer overheating scenario, showed that the aerogel-wrapped module reached the 60°C critical discharge temperature limit from 20°C in 4,680 s (78 minutes) under moderate driving heat generation at +35°C ambient, confirming that aerogel-based designs must incorporate provisions for warm-weather thermal management.

The comparative results provide a quantitative engineering basis for selecting and designing battery thermal management systems suited to Mongolian operating conditions. This work represents the first systematic module-level finite element comparison of these four strategies under the specific thermal conditions of Mongolia, addressing a gap in the existing engineering literature.

1. Introduction

1.1 Background and Motivation

The global transition away from fossil fuel-powered transportation represents one of the most significant engineering and policy challenges of the twenty-first century. Electric vehicles (EVs) have emerged as the primary technological solution for reducing greenhouse gas emissions from the transportation sector, with sales growing at an accelerating rate worldwide. More than half of all vehicles sold in China in 2024 were electric, and by 2030 Europe and the United States are targeting EV sales shares of approximately 60% and 20%, respectively [1]. However, the widespread adoption of EVs in cold-climate regions presents unique technical challenges that are not encountered in temperate or tropical environments.

Mongolia is one of the most extreme examples of a cold-climate inhabited zone. Located in the heart of Central Asia, Mongolia experiences harsh continental weather throughout most of the year. The historically lowest recorded temperature in Mongolia reached −58°C, and average January temperatures in Ulaanbaatar hover around −25°C, making it one of the coldest capital cities in the world [2]. These conditions place Mongolia among the most demanding environments globally for EV battery thermal management.

Lithium-ion batteries, like the lithium iron phosphate ($LiFePO_4$, or LFP) chemistry investigated in this thesis, are highly sensitive to temperature. The fundamental electrochemical processes that enable charge and discharge (lithium-ion diffusion, charge-transfer reactions, and electrolyte ionic conductivity) all slow dramatically as temperature decreases. At −20°C, the available energy from a lithium-ion cell is reduced to approximately 60% of its room-temperature capacity, and at temperatures approaching −40°C, power capability may be reduced by up to 80% or more [3]. Furthermore, charging a lithium-ion battery at sub-zero temperatures risks the deposition of metallic lithium on the graphite anode, a process known as lithium plating, which can permanently damage the cell and create a short-circuit hazard.

For Mongolian EV users, these degradation effects translate directly into practical problems: reduced driving range during cold months, difficulty starting the vehicle after overnight outdoor parking, slower charging, and accelerated battery ageing. For every degree Celsius below the optimal operating temperature of approximately +20°C, the driving range of an EV declines by approximately 0.8% [1]. Applied to Mongolian conditions, where the temperature may be 60°C below the optimal operating point, this

implies a theoretical driving range reduction of nearly 50%, severely limiting the practical utility of EVs without an effective thermal management system.

The LFP chemistry, as used by leading manufacturers such as CATL (Contemporary Amperex Technology Co. Limited) and BYD, is widely employed in electric vehicles because of its inherent thermal stability, long cycle life, and superior safety characteristics relative to other lithium-ion chemistries such as NMC (nickel manganese cobalt) and NCA (nickel cobalt aluminium). LFP cells do not undergo exothermic thermal runaway as readily as higher-energy-density chemistries, and they are less prone to oxygen release at elevated temperatures. However, LFP chemistry is not immune to the performance penalties associated with low temperatures, and the need for thermal management in cold climates is no less acute than for other chemistries.

This thesis is motivated by the necessity of systematically evaluating and comparing thermal management strategies for LFP battery modules under the specific climatic conditions of Mongolia. By conducting finite element thermal simulations in ANSYS Workbench, this study provides quantitative engineering data to support the design of EV battery packs suitable for deployment in one of the world's most challenging cold-climate environments.

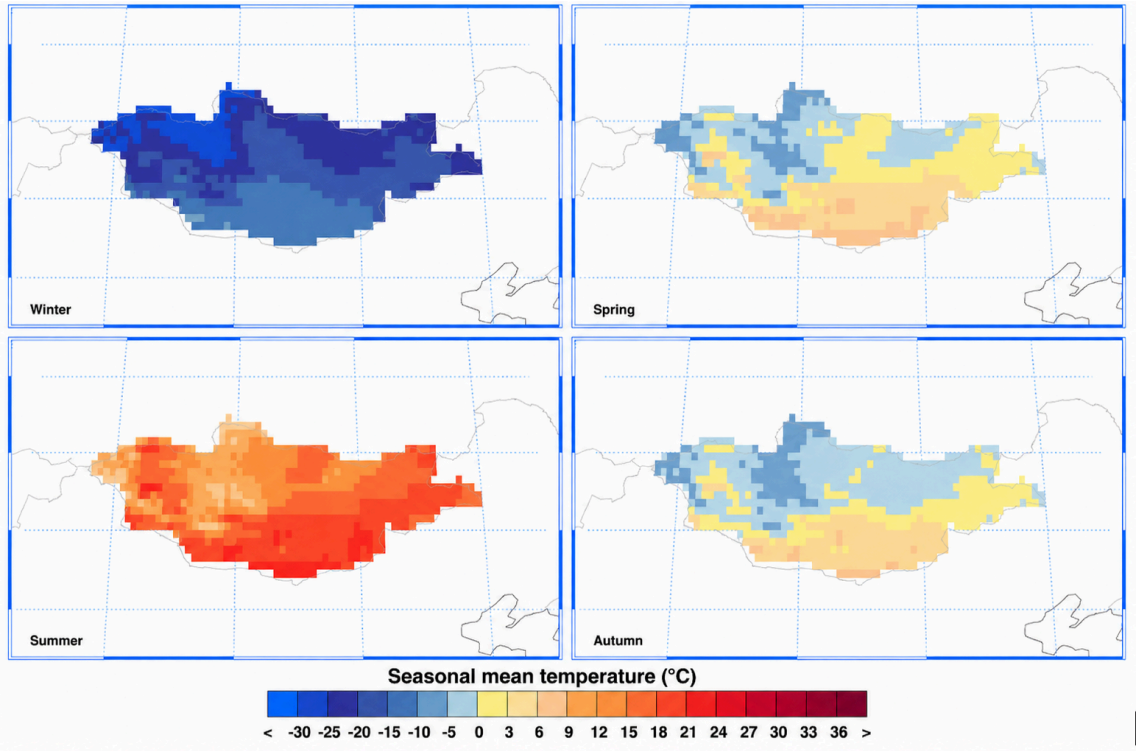


Fig.1: Seasonal mean temperature map of Mongolia

1.2 Problem Statement

The central problem addressed in this thesis is the degraded performance of an LFP battery module when exposed to ambient temperatures as low as −40°C without active or passive thermal management. Under such conditions, the module cannot deliver its rated capacity, accepts charging only at a severely reduced rate, and is at risk of permanent damage due to lithium plating on the graphite anode of individual cells [3,4]. To address this problem, this thesis evaluates the effectiveness of multiple thermal management strategies through simulation under Mongolian operating conditions, with particular focus on their performance limits.

Several thermal management strategies exist in the engineering literature and commercial practice, each with different operating principles, cost implications, energy consumption profiles, and suitability for extreme cold. These include passive insulation using aerogel blankets, external resistive heating via positive temperature coefficient (PTC) heater elements, internal alternating-current (AC) self-heating that exploits the battery's internal resistance, and passive thermal buffering using phase change materials (PCMs). While each strategy has been demonstrated individually under specific conditions, a direct, quantitative, module-level comparison under Mongolian operating conditions using a commercially representative cell geometry has not previously been reported. The selection of an appropriate thermal management strategy must also consider not only thermal performance but also energy consumption, cost, and ease of installation.

1.3 Research Objectives

The research objectives of this thesis are as follows:

Objective 1. To develop a representative three-dimensional CAD model of a 12S1P LFP battery module based on the CATL 100 Ah prismatic cell, including the geometric bodies for all four individual thermal management strategies (Systems A to D) and their combinations (System E), using Autodesk Inventor Professional 2026.

Objective 2. To define and justify appropriate material properties, boundary conditions, and heat generation parameters for each of the six simulation systems (Baseline and Systems A to E), grounded in existing literature and manufacturer specifications.

Objective 3. To conduct transient thermal finite element analyses in ANSYS Workbench 2025 R2 for simulation systems under system-specific boundary conditions: the Baseline and Systems A and D evaluate passive cold-resistance

performance, with the module starting at +20°C and cooling in a −40°C environment; Systems B and C evaluate active heating performance, with the module starting at −40°C and warming under applied heat input; and System E evaluates five sub-simulations combining passive and active components under cold-start (−40°C ambient) and summer overheating (+35°C ambient) conditions.

Objective 4. To compare the thermal performance of the four individual strategies and their combinations in terms of minimum cell temperature, maximum cell temperature, temperature uniformity across the module, and time required to reach safe operating temperature (0°C or above).

Objective 5. To assess the practical viability of each strategy for deployment in Mongolia, considering energy consumption, installation complexity, and behaviour across different seasonal conditions.

Objective 6. To identify the most suitable thermal management approach, or combination of approaches, for recommendation in the Mongolian cold-climate EV context.

1.4 Scope and Limitations

This study is conducted at the module level and analyses a single 12S1P battery module rather than a complete battery pack. This scope is appropriate for a first-order engineering assessment of thermal management strategy effectiveness, since the module is the fundamental repeating unit in a battery pack design. Pack-level scaling effects are discussed qualitatively in Chapter 5; however, module-to-module heat transfer, inter-module structural members, and pack-level thermal management hardware are outside the scope of this analysis.

The finite element analyses are performed using the ANSYS Student licence, which imposes a limit of 32,000 nodes. This constraint requires the use of a relatively coarse mesh with an element size of 7.4 mm. The mesh is sufficient to capture the global thermal behaviour of the module but may not resolve fine-scale thermal gradients within individual cell layers. The mesh size was validated by confirming that key temperature results had converged at this resolution.

Material properties are assigned as bulk homogeneous values based on published literature and manufacturer data. The internal electrochemical structure of the LFP cells, including electrode layers, separator, and current collectors, is not modelled explicitly. Instead, orthotropic thermal conductivity values representative of the layered

cell structure are applied at the cell-body level. This is a well-established approach in module-level battery thermal modelling [3].

The AC self-heating strategy is represented by an equivalent volumetric heat generation term within the cell bodies, corresponding to Joule heating produced by AC current flowing through the cells' internal resistance. The detailed circuit-level control strategy for AC self-heating is not modelled, as the focus of this thesis is on the thermal response of the module to the prescribed heat generation rate.

Due to software licence limitations, fluid dynamics and phase-change latent heat effects within the PCM are not modelled explicitly. The PCM is represented as a solid with effective thermal properties incorporating an elevated specific heat capacity. This is a conservative approximation, since the actual thermal performance of the PCM during phase transition would exceed that predicted by the solid-only model.

No active cooling solution is included in this thesis. The summer overheating scenario in System E5 is included solely to identify and quantify the overheating risk that aerogel insulation may present during warm-weather operation under driving conditions. This constitutes a finding of the study, not a problem to be resolved within its scope. The design of active cooling measures for warm-weather operation at the pack level is identified as a priority for future research.

1.5 Thesis Structure

This thesis is organised in accordance with the IMRaD structure recommended by GMIT and standard scientific reporting practice. Chapter 2 presents the State of the Art, reviewing the published literature on LFP battery technology, low-temperature degradation mechanisms, and existing thermal management strategies for EV batteries. Chapter 3 describes the Materials and Methods, detailing the battery module geometry, CAD development, ANSYS simulation setup, material properties, and the six simulation systems (Baseline and Systems A to E), including their boundary conditions and evaluation metrics. Chapter 4 presents the Results of all transient thermal simulations, organised by system and followed by a comparative summary and efficiency ranking. Chapter 5 provides the Discussion and Conclusions, interpreting the results in the context of Mongolian EV deployment and making recommendations for future work. Chapter 6 lists all references cited in the thesis. A Statutory Declaration is provided at the end of the document.

2. State of the Art

2.1 $LiFePO_4$ Battery Technology

The lithium iron phosphate battery, commonly designated as LFP from its chemical formula $LiFePO_4$, is a member of the lithium-ion battery family that uses lithium iron phosphate as the cathode active material and graphite as the anode. First commercialised in the early 2000s, LFP chemistry has gained significant traction in the EV market due to its strong safety profile, long cycle life, relatively low cost, and environmentally benign constituents. LFP cells do not contain cobalt, nickel, or manganese, which increase both cost and supply chain risk in NMC and NCA chemistries, and iron and phosphate are among the most abundant elements in the Earth's crust.

The electrochemical operation of an LFP cell is based on the intercalation and de-intercalation of lithium ions between the anode and cathode during cycling. During discharge, lithium ions migrate from the graphite anode through the liquid electrolyte and separator to the $LiFePO_4$ cathode, while electrons flow through the external circuit to perform electrical work. The nominal cell voltage of LFP is approximately 3.2 V, which is lower than NMC (3.7 V) but is accompanied by an exceptionally flat discharge curve, maintaining voltage close to the nominal value across most of the state of charge (SOC) range. This voltage flatness is advantageous for battery management systems (BMS), as it simplifies SOC estimation.

A key distinguishing characteristic of LFP chemistry is its inherent thermal stability. The iron-oxygen bonds in the olivine phosphate structure are stronger than the metal-oxygen bonds in layered oxide cathodes, requiring significantly higher temperatures to initiate exothermic decomposition. LFP cells exhibit no oxygen release and negligible exothermic reaction up to approximately 270°C, compared with onset temperatures of approximately 150 to 200°C for NMC chemistry [3]. This property makes LFP substantially safer under abuse conditions such as overcharge, external short circuit, and mechanical damage. For this reason, LFP has been selected by CATL for use in its standard-range battery packs and is widely deployed in electric buses, commercial vehicles, and energy storage applications where safety and longevity are prioritised over energy density.

The principal disadvantage of LFP relative to competing lithium-ion chemistries is its lower gravimetric and volumetric energy density. Typical LFP cells achieve energy densities of approximately 120 to 160 Wh/kg at the cell level, compared with 200 to 280

Wh/kg for modern NMC cells [3]. However, modern CATL cell-to-pack designs have substantially mitigated the volumetric penalty of LFP at the pack level by integrating cells directly into the pack and eliminating module-level packaging [3].

A second significant disadvantage of LFP for cold-climate applications is its particularly poor low-temperature performance. The flat discharge voltage plateau of LFP, while advantageous at room temperature, becomes a liability at low temperatures because voltage drops sharply at the beginning and end of discharge when temperature-induced resistance increases are most pronounced. Furthermore, the diffusivity of lithium ions within the LFP cathode structure is lower than in NMC at sub-zero temperatures, contributing to reduced power capability. Experimental results show that LFP cells at −10°C exhibit significantly lower discharge capacity compared with room-temperature performance, and the severity of this reduction increases with charge rate [4].

2.2 Effects of Low Temperature on Lithium-Ion Batteries

2.2.1 Performance Degradation at Low Temperatures

The performance of lithium-ion batteries, and by extension LFP cells, is critically dependent on temperature. Three primary physical mechanisms are responsible for low-temperature performance degradation: reduced electrolyte ionic conductivity, increased charge-transfer resistance at the electrode-electrolyte interfaces, and reduced lithium-ion diffusivity within the solid electrode materials [3].

The electrolyte of a lithium-ion battery consists of a lithium salt, typically $LiPF_6$, dissolved in an organic solvent mixture. Its ionic conductivity is strongly temperature-dependent and decreases as temperature falls because solvent viscosity increases and the mobility of lithium ions is reduced. At temperatures approaching −40°C, conventional carbonate-based electrolytes may approach their freezing point, at which point ionic conductivity collapses and the cell becomes non-functional. For the same applied current, the available energy from a $LiFePO_4$ cell at −20°C is approximately 60% of its room-temperature value, as reported for prismatic LFP cells tested at discharge currents of 50 A, 100 A, and 300 A [3].

Charge-transfer resistance at the electrode-electrolyte interface increases substantially at low temperature. This resistance arises from the activation energy required for lithium ions to cross the interface between the electrolyte and the electrode surface. For cells with $LiBF_4$-based electrolyte, the charge-transfer resistance increases

significantly as temperature drops below −20°C [3]. This is particularly problematic during charging at low temperature, because the high interface resistance and the slow diffusion of lithium ions into the graphite anode can cause metallic lithium to deposit on the anode surface instead of intercalating into the graphite structure.

Reduced lithium-ion diffusivity within the solid electrode materials is the third contributing factor. As temperature decreases, the diffusion coefficient of lithium ions in both the graphite anode and the LFP cathode decreases, leading to concentration gradients within the electrode particles that limit the rate at which lithium can be stored and released. The diffusivity of lithium ions in graphite decreases dramatically below 0°C, and delithiated graphite in the discharged state exhibits lower diffusivity than lithiated graphite in the charged state [3]. This asymmetry means that charging a deeply discharged cell at low temperature is especially susceptible to lithium plating.

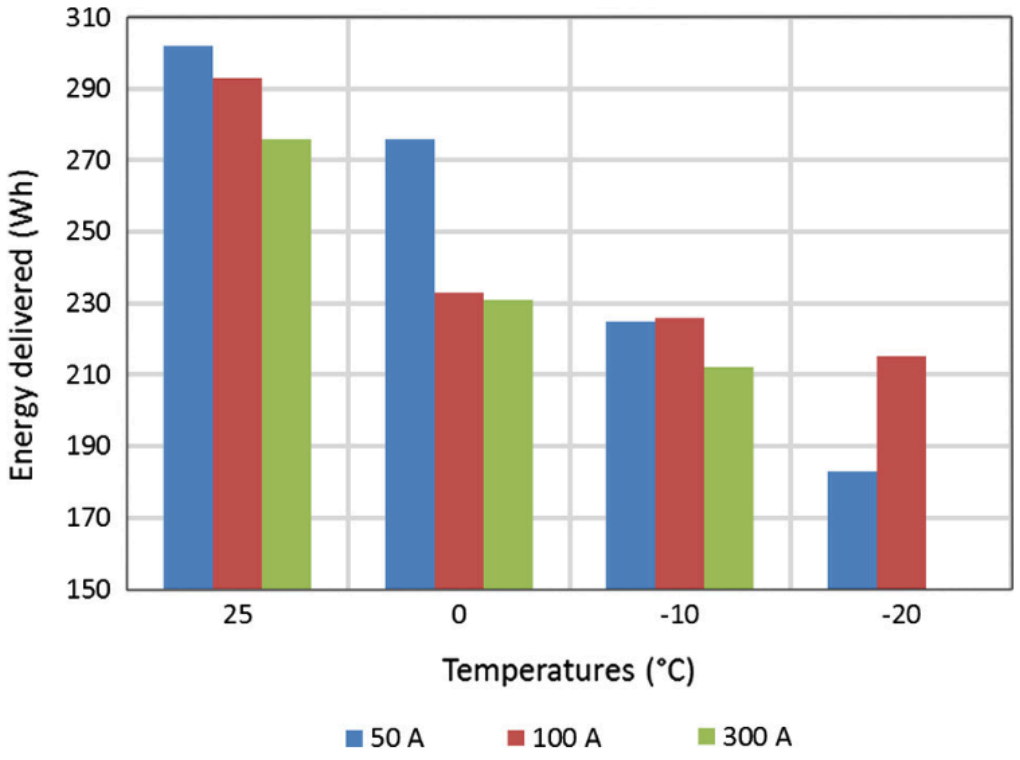


Fig.2: Discharge capacity as a function of temperature for LFP cells, illustrating the severe performance reduction at sub-zero temperatures.

2.2.2 Aging Mechanisms at Low Temperatures

In addition to immediate performance degradation, low-temperature operation significantly accelerates irreversible aging in lithium-ion cells. Lithium plating is widely regarded as the dominant degradation mechanism at sub-zero temperatures [3]. When charging occurs below approximately 0°C, the reduced diffusion rate of lithium ions within the graphite anode, combined with increased charge-transfer resistance, leads to a mismatch between lithium intercalation and supply. This imbalance promotes the deposition of metallic lithium on the anode surface rather than its insertion into the graphite structure. The deposited lithium typically forms either dendritic structures, which may penetrate the separator and cause internal short circuits, or mossy deposits, which irreversibly consume active lithium and reduce usable capacity.

Experimental investigations on graphite-LFP cells employing a 1 mol $LiPF_6$ electrolyte in ethylene carbonate/diethylene carbonate and cycled at −10°C indicate that the severity of low-temperature degradation is strongly dependent on charge rate. At low C-rates, the impact of temperature is less pronounced, suggesting that kinetic limitations remain partially manageable. However, at higher charge rates, the overpotential increases substantially, leading to severe performance degradation and enhanced lithium plating. Surface characterisation using X-ray photoelectron spectroscopy (XPS) further confirms the formation of a thicker solid electrolyte interphase (SEI) layer under low-temperature cycling conditions, indicating intensified parasitic side reactions [4].

The solid electrolyte interphase (SEI) is a passivation layer formed at the anode-electrolyte interface during initial cycling and continues to evolve throughout the cell lifetime. Capacity fade arises as SEI growth irreversibly consumes cyclable lithium. At low temperatures, the SEI exhibits reduced mechanical stability and is more prone to fracture during volumetric changes associated with lithiation and delithiation. Repeated cracking exposes fresh electrode surface to the electrolyte, triggering additional SEI formation and further lithium loss [3].

The combined effects of lithium plating and accelerated SEI growth result in irreversible capacity loss at rates significantly higher than those observed at room temperature. In the context of Mongolian EV applications, where batteries are routinely subjected to repeated cold starts and low-temperature charging cycles, accelerated degradation represents a critical reliability and lifetime limitation. Consequently, maintaining cell temperature within a safe operating range prior to charging or high-current discharge is

not merely beneficial but essential, reinforcing the necessity of an effective thermal management system.

2.3 Thermal Management Strategies for EV Batteries

2.3.1 Passive Insulation with Aerogel (System A)

Aerogel is an ultralow-density, highly porous solid material characterised by a three-dimensional silica network with pore sizes in the nanometre range. Its exceptional thermal insulation properties arise from the combination of a very low solid thermal conductivity (due to the thin silica strands of the network), suppressed gaseous thermal conductivity (due to the nanoporous structure operating below the mean free path of air molecules), and minimal convective heat transfer within the pores. Commercial silica aerogel insulation blankets achieve thermal conductivities in the range of 0.014 to 0.020 W/(m·K) at atmospheric pressure and room temperature, compared with 0.030 to 0.038 W/(m·K) for conventional glass wool and 0.029 to 0.047 W/(m·K) for expanded polystyrene foam [5,6,7].

In the context of EV battery thermal management, aerogel insulation is employed as a passive strategy to reduce heat exchange between the battery module and the ambient environment. During cold weather operation, the insulation slows the rate at which heat generated by the battery during discharge is lost to the cold surroundings, allowing the cells to retain warmth for longer after the vehicle has been parked. During a cold soak, the insulation delays the rate of temperature decrease, extending the period during which the battery remains within its safe operating range.

The principal advantage of aerogel insulation is its purely passive nature: it requires no electrical power, has no moving parts, and introduces no additional failure modes into the battery system. It is also lightweight relative to its insulating performance. However, aerogel insulation has a significant limitation for cold-climate applications: it provides no active heat input and cannot raise the battery temperature above the ambient level. In a Mongolian winter scenario where the ambient temperature is −40°C, the battery temperature will inevitably converge toward −40°C over a sufficiently long soak period regardless of the insulation quality.

A further concern with aerogel insulation in a Mongolian context is the dual-season performance penalty. During driving under high-load conditions, the same insulation that prevents cold-weather heat loss will also prevent the battery from dissipating heat to the environment, potentially leading to overheating. This thesis includes a summer

overheating simulation (System E5) to quantify this risk. The thermal conductivity value of aerogel used in this study is 0.016 W/(m·K), based on published manufacturer specifications for silica aerogel blanket material [5].

2.3.2 External PTC Resistive Heating (System B)

Positive temperature coefficient (PTC) heaters are a class of ceramic resistive heating elements whose electrical resistance increases sharply with temperature above a threshold known as the Curie temperature. This self-regulating property means that PTC heaters automatically reduce their power output as they approach a target temperature, making them inherently safe and straightforward to control without additional feedback systems. PTC heater elements are commonly manufactured from barium titanate-based ceramics doped with rare-earth elements to set the desired Curie temperature.

External PTC heaters are a standard solution in EV battery thermal management for cold conditions. They are typically implemented as thin, flat heating plates sandwiched between cells or attached to module surfaces to provide uniform heat distribution. In low-temperature operation, the thermal management system activates these heaters to raise battery temperature before driving or charging, often switching between waste heat recovery (when available) and direct electric heating depending on battery state of charge and operating temperature [1,8].

For this study, a PTC heater plate with overall dimensions of 404.14 mm × 200.33 mm × 10 mm, including a concave pocket of 352.14 mm × 146.33 mm × 6 mm machined into the outer face, is modelled applied to one large face of the battery module. A rated heater power of 150 W was selected to represent a compact 12 V automotive PTC heater module, corresponding to a current draw of 150 W / 12 V = 12.5 A from the vehicle's auxiliary electrical system, which is within the standard continuous current rating of a 12 V automotive auxiliary circuit [1,8].

The minimum theoretical energy required to warm all twelve cells from −40°C to 0°C, assuming no heat loss, is estimated from the total cell thermal mass. With a homogenised cell density of 2,300 kg/m^3 and cell volume of 0.001146 m^3, the mass per cell is 2.636 kg, giving a total cell mass of 12 × 2.636 = 31.63 kg. The minimum energy is therefore $Q = m \times c_p \times \Delta T = 31.63 \times 1{,}200 \times 40 = 1{,}518{,}240$ J ≈ 1.52 MJ, requiring a minimum warm-up time of Q / P = 1,518,240 / 150 ≈ 10,122 s ≈ 2.8 hours under adiabatic conditions. This confirms that 150 W represents a conservative lower-bound scenario for this module size and temperature differential; convective losses at −40°C

ambient further extend the actual warm-up requirement beyond this theoretical minimum.

The primary limitation of external surface heating is that heat is applied only at the module surface and must conduct through the relatively low through-plane thermal conductivity of the LFP cells (k_z = 0.47 W/(m·K)) to reach the interior of the module. This introduces a temperature gradient across the module in the stacking direction, with cells adjacent to the heater warming faster than cells on the opposite face. Temperature uniformity across the module is therefore a key evaluation metric for System B.

2.3.3 Internal AC Self-Heating (System C)

Internal alternating current (AC) self-heating is a technique in which an alternating current is passed through battery cells, exploiting their internal resistance to generate Joule heat uniformly within the cell volume. The concept of using alternating current to heat automotive batteries at low temperature was first demonstrated by Stuart and Hande [9], who showed that an AC current supplied from an external source could effectively warm battery packs in hybrid electric vehicles without the electrochemical damage associated with direct current charging at sub-zero temperatures. Their work established that AC stimulation at an appropriate frequency does not induce irreversible lithium reactions at the cell electrodes, making it fundamentally safer than direct current charging below 0°C.

The physical basis of AC self-heating is straightforward: when an alternating current of root-mean-square (RMS) amplitude I passes through a cell with internal resistance R, the power dissipated as heat is $P = I^2 \times R$. The use of alternating rather than direct current is critical for lithium-ion cells, because direct current charging at sub-zero temperatures drives lithium plating at the graphite anode. An alternating current at sufficiently high frequency does not produce a net lithium-ion flux at the electrode surface within each cycle, and therefore does not cause plating. Ji and Wang [10] identify AC self-heating as an effective warm-up approach and establish that operating frequencies above approximately 10 Hz are sufficient to prevent net lithium deposition while still generating useful resistive heating.

A related but distinct approach was later demonstrated by Wang et al. [11], who developed a specialised lithium-ion cell containing an embedded internal nickel foil resistance element. By applying a direct current voltage of 0.4 V across the nickel foil, they achieved rapid warming of an NMC cell from −20°C to 0°C in approximately 19.5 seconds, from −30°C to 0°C in approximately 29.6 seconds, and from −40°C to 0°C in

approximately 42.5 seconds. Although the heating rate is impressive, this approach requires a non-standard cell construction with an internal foil not present in commercially available prismatic LFP cells such as the CATL 100 Ah cell used in this study. This technique is noted here as a relevant variant confirming the feasibility of rapid internal heating, but is not the basis of the AC self-heating strategy modelled in this thesis.

For this simulation study, the AC self-heating effect is modelled as an equivalent internal volumetric heat generation rate applied uniformly to all twelve cell bodies. At −39°C, the internal resistance of an LFP cell increases substantially compared to room temperature. Based on published impedance spectroscopy data for LFP cells at low temperatures [3], the internal AC resistance of a 100 Ah LFP cell at −39°C is estimated at approximately 25 mΩ (0.025 Ω). Applying an RMS current of 50 A at AC frequency, the heat generated per cell is $P_{cell} = I^2 \times R = 50^2 \times 0.025 = 62.5$ W per cell. Across twelve cells, the total heat generation is 750 W, five times greater than the external heater in System B.

The key thermal advantage of AC self-heating over external heating is that all twelve cells generate heat internally and simultaneously, so temperature non-uniformity across the module is far lower than in System B. This uniformity is critical for module longevity, since differential cell temperatures lead to differential ageing and cell-to-cell capacity mismatch over repeated cycles.

2.3.4 Phase Change Materials (System D)

Phase change materials (PCMs) are substances that store and release thermal energy during the process of melting and solidification, exploiting the latent heat associated with the solid-liquid phase transition. During melting, a PCM absorbs a large quantity of heat while maintaining a nearly constant temperature equal to its melting point; during solidification, it releases the same quantity of heat. This isothermal buffering characteristic makes PCMs attractive as passive thermal management elements in battery systems: they can absorb rapid heat generation from the battery during high-rate discharge without allowing cell temperature to spike sharply.

Paraffin waxes are the most widely studied PCM class for battery thermal management applications. The designation RT35 refers to a commercial paraffin-based PCM produced by Rubitherm GmbH (Germany) with a nominal melting temperature of approximately 35°C and a latent heat of fusion of approximately 160 kJ/kg [12]. RT35 is selected for applications where the battery must be maintained below approximately 40°C, corresponding to the upper boundary of the safe operating temperature range for

LFP cells. However, for a cold-climate application such as Mongolia, a PCM with a 35°C melting point provides no latent heat benefit at winter operating temperatures: at −40°C the PCM is entirely solidified. In this regime the PCM functions only as a solid thermal mass, slowing the rate of temperature change in the adjacent cells by virtue of its specific heat capacity.

In this study, the PCM body (RT35 paraffin) is placed on the large module face opposite to the heating plate, with dimensions of 404.14 mm × 200.33 mm × 3 mm. The volume, mass, and theoretical heat storage capacity of the PCM slab are:

V_{PCM} = 0.40414 m x 0.20033 m x 0.003 m = 0.000243 m^3

m_{PCM} = V x rho = 0.000243 m^3 x 880 kg/m^3 = 0.214 kg

$Q_{sensible}$ (-39ºC to 35ºC) = 0.214 x 2,500 x 74 = 39,590 J (approx. 39.6 kJ)

Q_{latent} (full melt) = 0.214 x 160,000 = 34,240 J (approx. 34.2 kJ)

Q_{total} = approx. 73.8 kJ

This thermal storage capacity confirms that the 3 mm PCM slab provides a modest but measurable thermal buffer. Key material properties of RT35 PCM used in this study are: thermal conductivity k = 0.2 W/(m·K), density ρ = 880 kg/m^3, and effective specific heat capacity c_p = 2,500 J/(kg·K). The elevated effective specific heat capacity partially accounts for the latent heat contribution distributed across the melting temperature range, consistent with the effective medium approximation used for the solid-only PCM model in ANSYS. This is a conservative simplification; the actual thermal performance of the PCM during phase transition would exceed that predicted by a purely solid model, since the model neglects isothermal latent heat absorption at 35°C [12].

Despite its limitations in pure cold-soak conditions, PCM is of value as part of a combined thermal management strategy. When the battery approaches operating temperature (near 35°C) during discharge under moderate driving conditions, the PCM absorbs excess heat isothermally, preventing overtemperature events more effectively than a solid thermal mass of equivalent thickness. However, as the results of System E3 and E4 demonstrate, in cold-start scenarios the cold PCM mass acts as a heat sink rather than a heat source, absorbing energy that would otherwise warm the cells.

2.4 Mongolian Climate Context

Mongolia occupies a unique climatic position as one of the world's most extreme continental climates. Landlocked in the heart of Central Asia at an average elevation of approximately 1,580 m above sea level, Mongolia experiences a semi-arid to arid

steppe climate characterised by very cold winters, warm summers, and an exceptionally wide annual temperature range [13]. The lowest temperature ever recorded in Mongolia reached −58°C [2], and the capital city Ulaanbaatar consistently records average January temperatures between −20°C and −30°C, with extreme overnight minima regularly reaching −35°C to −40°C. Ulaanbaatar is widely recognised as the world's coldest capital city, with a mean annual temperature below −1°C [14].

These temperatures are not merely statistical extremes confined to remote rural areas; they are routinely experienced by the general urban population of Ulaanbaatar during winter. An electric vehicle parked outdoors overnight in Ulaanbaatar in January would routinely have its battery cooled to the −30°C to −40°C range by morning. The design temperature of −40°C adopted as the cold-soak ambient condition in this study is therefore not a worst-case extreme but a realistic operational condition encountered by EV users in Ulaanbaatar and the surrounding region during a typical January night.

The wide seasonal temperature swing, from approximately −40°C in winter to +38°C in summer, defines the environmental range within which any electric vehicle deployed in Mongolia must operate. The primary challenge addressed by this thesis is cold-weather performance: raising battery temperature to a safe level before driving or charging. However, the aerogel insulation adopted for cold-weather protection also reduces heat dissipation during warmer operation. A summer overheating scenario is therefore included in System E5 to identify and quantify this risk at the module level. The design of appropriate cooling strategies for warm-weather operation is outside the scope of this study and is identified as a direction for future work.

For Mongolian EV users, the practical consequences of cold-temperature battery degradation are severe. At −40°C, available battery power may be reduced by up to 80% or more relative to room temperature [3], and charging is not safely possible without prior thermal management due to the risk of lithium plating. For every degree Celsius below the optimal operating temperature of approximately +20°C, driving range declines by approximately 0.8% [1]. Applied to a −40°C Mongolian winter start, this equates to a theoretical range reduction of nearly 50%, compounding the urgency of identifying effective thermal management solutions for this environment.

2.5 Summary and Research Gap

The reviewed literature establishes that lithium-ion batteries, including LFP chemistry, suffer severe and potentially irreversible performance degradation at the sub-zero temperatures characteristic of the Mongolian winter. Three fundamental physical

mechanisms drive this degradation: reduced electrolyte ionic conductivity, increased charge-transfer resistance at the electrode-electrolyte interfaces, and reduced lithium-ion diffusivity within the solid electrode materials. These effects compound at temperatures approaching −40°C to produce dramatic reductions in available power and capacity, while simultaneously creating conditions for lithium plating during charging that permanently reduce cell capacity and pose safety hazards.

Four distinct thermal management strategies are available to mitigate low-temperature degradation, each with fundamentally different operating principles and trade-offs. Passive aerogel insulation slows thermal equilibration with the cold environment but cannot generate heat, and is therefore insufficient as a standalone winter strategy under conditions as extreme as the Mongolian winter. External PTC resistive heating provides active heat input from a surface-mounted plate, but its effectiveness is limited by the need for heat to conduct inward across the full module width through the low through-plane thermal conductivity of the LFP cells. Internal AC self-heating generates heat uniformly within every cell simultaneously, offering the fastest and most thermally uniform warming response but requiring energy drawn from the traction battery. Phase change material buffering provides passive thermal mass and isothermal heat absorption near the melting point, contributing meaningful thermal buffering under charging and high-rate discharge conditions, but contributing only solid thermal mass at the extreme cold temperatures of Mongolian winters.

Despite a substantial body of research on each of these strategies individually, no published study has conducted a systematic, module-level, transient thermal finite element comparison of all four strategies simultaneously for a specific, commercially representative LFP module geometry under Mongolian operating conditions. This absence constitutes the research gap directly addressed by this thesis. The study presented here applies all four strategies, and their combinations, to a single 12S1P CATL 100 Ah prismatic LFP module and provides quantitative engineering data to support the design of effective battery thermal management systems for electric vehicles deployed in Mongolia and comparable cold-climate environments.

3. Materials and Methods

3.1 Battery Cell and Module Specifications

The battery cell selected for this study is the CATL (Contemporary Amperex Technology Co. Limited) LFP prismatic cell with a nominal capacity of 100 Ah and a nominal voltage of 3.2 V. This cell is representative of the prismatic LFP format widely deployed in contemporary electric vehicles, including those manufactured by BYD and other original equipment manufacturers. The complete cell specifications used in this study are summarised in Table 1 [15,16].

Table 1: CATL 100 Ah LFP prismatic cell specifications and thermal properties used in ANSYS.

Parameter	**Value**	**Unit**
Nominal voltage	3.2	V
Nominal capacity	100	Ah
Nominal energy	320	Wh
Cell length (X, face width)	200.33	mm
Cell height (Y, face height)	172.2	mm
Cell thickness (Z, stacking)	33.22	mm
Cell mass (approximate)	2.6	kg
Chemistry	$LiFePO_4$ (LFP)	-
Format	Prismatic (Al casing)	-
Maximum charge temperature	45	°C
Minimum charge temperature	0	°C
Maximum discharge temperature	60	°C
Minimum discharge temperature	−20	°C
Density (homogenised, for ANSYS)	2,300	kg/m^3
Specific heat capacity	1,200	J/(kg·K)
Thermal conductivity, in-plane (X, Y)	20	W/(m·K)
Thermal conductivity, through-plane (Z)	0.47	W/(m·K)

The thermal properties listed in Table 1 require further explanation because they are not uniform in all directions. The LFP prismatic cell is a layered structure comprising

alternating sheets of cathode, separator, and anode materials stacked inside an aluminium casing. Heat flows more easily along the plane of the electrode layers (in the X and Y directions, parallel to the large face) than across the layers (in the Z direction, the stacking direction). This directional difference in thermal conductivity is described as orthotropic thermal conductivity. The in-plane value of 20 W/(m·K) reflects the contribution of the metallic aluminium and copper current collectors, which are highly conductive and run parallel to the electrode layers. The through-plane value of 0.47 W/(m·K) reflects the much lower conductivity of the polymer separator and electrode coating layers that must be crossed in the Z direction. These values are applied as orthotropic thermal conductivity in ANSYS Engineering Data and are consistent with values reported in the literature for prismatic LFP cells [3].

The battery module investigated in this thesis consists of twelve cells arranged in a 12-series, 1-parallel (12S1P) configuration. The cells are stacked along their thickness direction (Z-direction, 33.22 mm per cell). In the CAD model, the cells are placed in direct face-to-face contact without explicit thermal interface material bodies between them, as described in Section 3.2. The resulting module stacking length in the CAD geometry is 12 × 33.22 mm = 398.64 mm. The cross-section perpendicular to the stacking direction corresponds to the cell face of 200.33 mm (X) × 172.2 mm (Y). The module configuration parameters are summarised in Table 2.

Table 2: Battery module configuration parameters.

Parameter	**Value**	**Unit**
Configuration	12S1P	-
Number of cells	12	-
Module nominal voltage	38.4	V
Module nominal capacity	100	Ah
Module nominal energy	3.84	kWh
Module stacking length (CAD)	398.64	mm
Module face width (X)	200.33	mm
Module face height (Y)	172.2	mm

The 12S1P configuration produces a module nominal voltage of 12 × 3.2 V = 38.4 V and a nominal energy of 12 × 320 Wh = 3.84 kWh. A complete electric vehicle battery pack would consist of multiple such modules connected in series or parallel to achieve the required pack voltage and energy capacity; however, as noted in Section 1.4, this study analyses the thermal behaviour of a single module.

3.2 CAD Geometry Development

Three-dimensional CAD models of the battery module and associated thermal management hardware were developed using Autodesk Inventor Professional 2026. The modelling approach is described below for the baseline module geometry and for each thermal management strategy addition.

The baseline module geometry consists of twelve cell bodies, each modelled as a solid rectangular prism with dimensions 200.33 mm × 172.2 mm × 33.22 mm, arranged in direct face-to-face contact along the stacking direction (Z). Two terminal bodies are attached to the top face of each cell: a positive terminal modelled as an aluminium block of 20 mm × 20 mm × 3 mm, and a negative terminal modelled as a copper block of 22 mm × 20 mm × 3 mm. The terminals protrude above the top cell face and represent the current-carrying connectors of the cell.

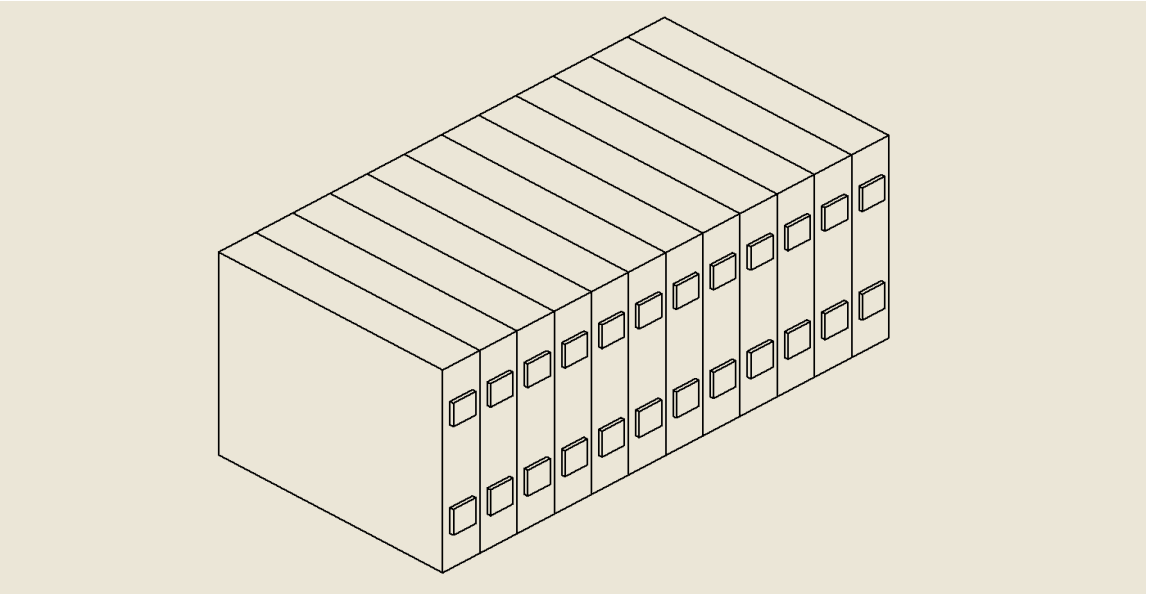


Fig.3: 12S1P battery module assembly showing all twelve stacked cell bodies and terminal blocks, baseline geometry.

Cell-to-cell contact is modelled as direct face-to-face contact without an explicit thermal interface material body between adjacent cells. While in physical battery assemblies a thin thermal interface material pad (approximately 0.5 mm compressed thickness) is typically applied between adjacent cells to reduce contact thermal resistance and fill surface imperfections, modelling these sub-millimetre layers as solid bodies produces extremely flat finite elements with aspect ratios exceeding 18:1 at the 7.4 mm mesh element size required by the ANSYS Student licence node count limit. Such elements cause poor mesh quality and convergence issues in ANSYS. The thermal resistance of the interface is therefore accounted for by applying a thermal contact conductance of 6,000 W/(m^2·K) to each cell-to-cell contact pair in ANSYS Mechanical, as described in Section 3.3.4. This conductance value is mathematically equivalent to the thermal resistance of a 0.5 mm pad with thermal conductivity k = 3.0 W/(m·K), since $h_c = k / t = 3.0 / 0.0005 = 6{,}000$ W/(m^2·K) [17].

For System A (passive aerogel insulation), a solid aerogel body enclosing the entire module was modelled, with a uniform aerogel thickness of 7.5 mm on all six external faces of the module. The module is completely enclosed within the aerogel envelope, reflecting the practical installation approach of wrapping the battery module in aerogel blanket material. The aerogel body was modelled as a single hollow rectangular shell surrounding the module, sharing the outer surfaces of the module cell stack at the inner boundary.

For System B (external PTC resistive heating), a PTC heater plate body was modelled and placed in contact with one large face of the module (the X-Z plane face at Y = 0). The heater plate has overall dimensions of 404.14 mm (Z) × 200.33 mm (X) × 10 mm (Y), including a concave pocket of 352.14 mm × 146.33 mm × 6 mm machined into the outer face. The pocket geometry represents the recessed cavity present in commercial PTC heater plates, which reduces material volume and improves airflow for cooling in summer operation. The flat inner face of the heater plate is placed directly against the module face. The 404.14 mm length of the heater plate corresponds to the fully designed physical assembly length including the inter-cell thermal interface material layers, providing complete coverage of the module face.

For System C (internal AC self-heating), no additional geometric bodies were required. The AC self-heating effect is represented entirely by a volumetric internal heat generation boundary condition applied directly to the existing cell bodies in ANSYS Mechanical, as described in Section 3.3.4.

For System D (phase change material buffer), a solid RT35 paraffin body was modelled as a flat rectangular slab placed in contact with the large module face opposite to the heater plate face (the X-Z plane face at Y = 172.2 mm). The PCM slab dimensions are 404.14 mm (Z) × 200.33 mm (X) × 3 mm (Y). This placement ensures that the PCM is in thermal contact with all twelve cells simultaneously through the largest available module face. The 3 mm thickness was selected to provide a meaningful thermal buffer mass without excessive volume.

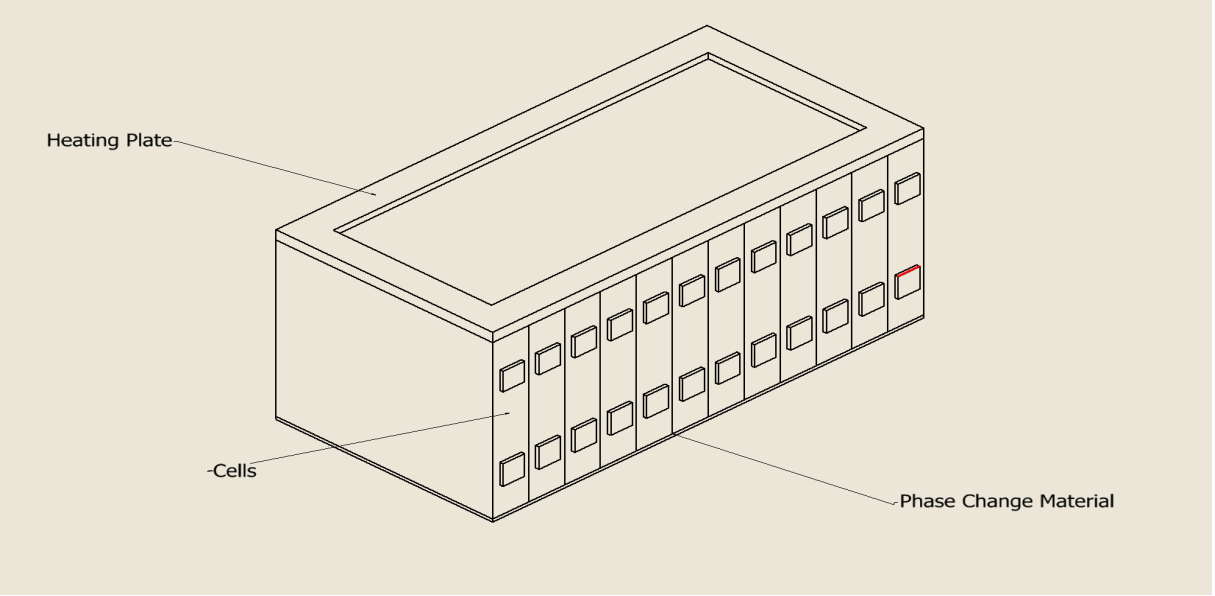


Fig.4: CAD assembly model of the battery module with thermal management components. The heater plate is shown on the upper face and the PCM slab on the lower face.

The completed CAD assemblies were exported from Autodesk Inventor Professional 2026 as STEP AP214 files (.step) for import into ANSYS Workbench. A separate STEP file was prepared for each system, with only the geometric bodies relevant to that strategy included in the assembly.

3.3 ANSYS Finite Element Analysis Setup

Transient thermal finite element analyses were conducted using ANSYS Workbench 2025 R2 with the Transient Thermal analysis system. Six separate Transient Thermal systems were created within the same Workbench project: a Baseline system representing the unprotected 12S1P module with no thermal management strategy, and five strategy systems designated System A through System E. Two distinct test types are used depending on the physical mechanism being evaluated. Heat retention

tests begin with the module at a warm initial temperature of +20°C and monitor how quickly the module cools in a −40°C ambient environment; the primary metric is how long the minimum cell temperature remains above 0°C (the safe charging threshold). Heat-up tests begin with the module at −40°C and apply an active heat source; the primary metric is how quickly the minimum cell temperature rises above 0°C. The Baseline, System A, and System D use heat retention test conditions. Systems B and C use heat-up test conditions. System E combines components from the individual strategies in five sub-simulations to identify the most effective and energy-efficient overall approach, and also examines overheating risk during warm-weather operation.

3.3.1 Geometry Import and Meshing

The STEP geometry files were imported into ANSYS Workbench via the Geometry cell of each Transient Thermal system. The geometry was opened in Ansys Discovery, where Shared Topology was applied to the multi-body assembly. Shared Topology merges the mesh at the interfaces between adjacent bodies, producing a conformal mesh with shared nodes at all internal contact faces. Without Shared Topology, each body would be meshed independently with no shared nodes at interfaces, and thermal contact conductance assignments would be required for every internal interface. With Shared Topology applied, heat conduction between bodies in direct solid contact (such as cell-to-cell contact in the stacked module or cell-to-aerogel contact in System A) is handled by direct node-to-node conduction through the shared mesh, which is the most accurate representation. Thermal contact conductance is then applied only to the interfaces that represent physical TIM layers, as described in Section 3.3.4.

The mesh was generated using the ANSYS Mechanical default patch-conforming meshing algorithm, which produces tetrahedral elements suitable for complex-shaped bodies such as the heater plate with its concave pocket. A uniform element size of 7.4 mm was applied globally to all bodies in each system. This element size was selected as the largest value that produces a mesh that remains within the 32,000 node limit imposed by the ANSYS Student licence across all six systems. The resulting node counts for all six systems were confirmed to be within this limit. The 7.4 mm element size is sufficient to capture the global temperature distribution and warm-up rates of the module, which vary over length scales of tens to hundreds of millimetres rather than at the sub-millimetre scale of individual electrode layers.

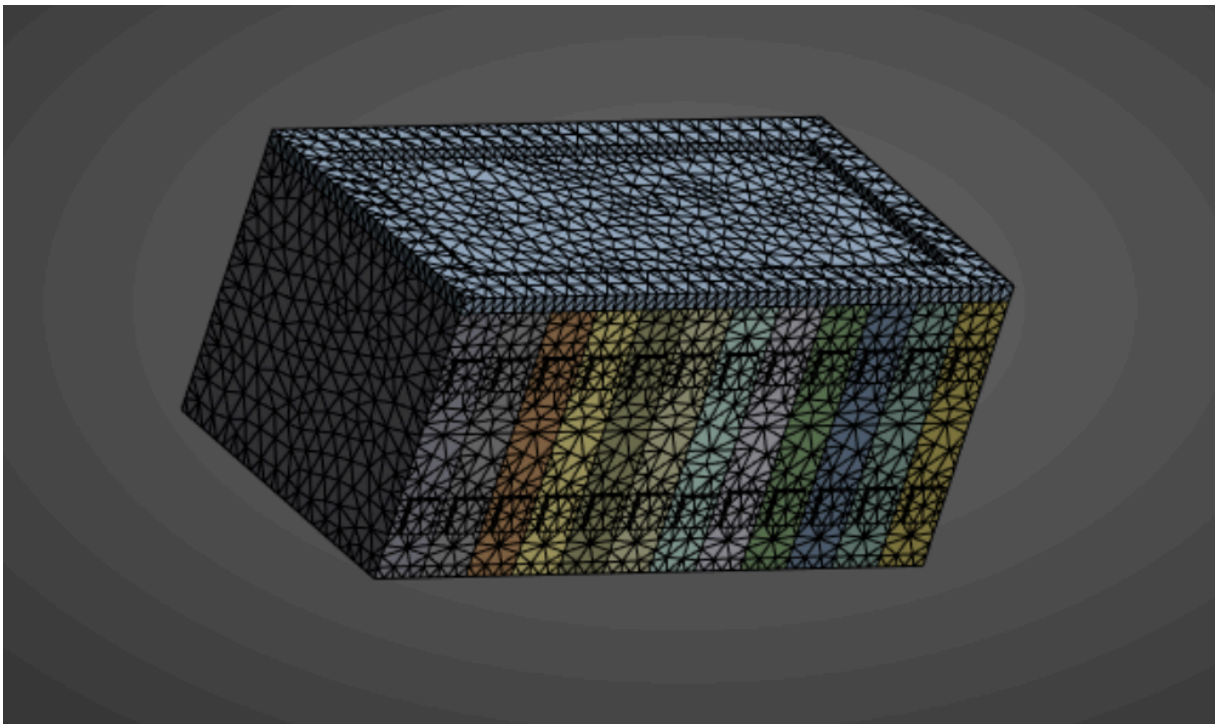


Fig.5: Finite element mesh of the battery module and heater plate (System B). The mesh was generated with a global element size of 7.4 mm.

Mesh quality was assessed using the Skewness and Aspect Ratio metrics in ANSYS Mechanical. Skewness values below 0.9 and aspect ratios below 10 are generally considered acceptable for thermal analyses, where temperature gradients are relatively smooth compared to structural analyses. The mesh met these criteria for all six systems. The use of contact conductance rather than solid TIM bodies eliminated the high-aspect-ratio elements that would otherwise arise from the sub-millimetre TIM thickness.

3.3.2 Material Properties

Material properties were defined in ANSYS Engineering Data and assigned to the corresponding bodies in each system. All material properties were sourced from published manufacturer datasheets or peer-reviewed literature and are summarised in Table 3. Where literature sources report a range of values, the midpoint or most commonly cited representative value was used.

Table 3: Material properties assigned in ANSYS Engineering Data. Effective c□ of RT35 accounts for latent heat contribution distributed across the melt range.

Material / Component	Density (kg/m³)	Sp. Heat (J/(kg·K))	Th. Conductivity (W/(m·K))
LFP cell body	2,300	1,200	$k_x = k_y = 20$ (in-plane)$k_ϱ = 0.47$ (through-plane)
Al positive terminal	2,700	900	160
Cu negative terminal	8,960	385	400
Aerogel blanket (Cryogel Z)	150	1,050	0.016
PTC heater plate (Al alloy)	2,700	900	160
RT35 PCM (Rubitherm)	880	2,500 (effective)	0.2

The thermal conductivity of the LFP cell body is defined as orthotropic, with separate values for the in-plane directions (X and Y) and the through-plane direction (Z). In ANSYS Engineering Data, orthotropic thermal conductivity is specified by entering separate k values for each coordinate axis. The in-plane value of 20 W/(m·K) is governed by the aluminium and copper current collectors, while the through-plane value of 0.47 W/(m·K) is governed by the polymer separator and active electrode material [3].

The positive and negative terminal bodies are assigned standard material properties for aluminium alloy and copper, respectively, as listed in Table 3. The terminals are included in the model for geometric completeness but their contribution to the total thermal mass of the module is small relative to the cell bodies.

The PTC heater plate body is assigned the properties of an aluminium alloy, representing the aluminium shell structure of the plate. The actual PTC ceramic heating elements within the plate are not modelled as separate bodies; instead, the heat they generate is applied as a boundary condition on the plate surface, as described in Section 3.3.4. The thermal properties of the aluminium shell govern the conduction of heat from the plate inner face through the plate body to the module contact face.

The effective specific heat capacity of RT35 PCM is set to 2,500 J/(kg·K), which is higher than the bulk solid specific heat of paraffin (approximately 1,800 to 2,000 J/(kg·K)). This elevated value uses the effective medium approach to partially account

for the latent heat of fusion (approximately 160 kJ/kg at 35°C) distributed across the melting temperature range in the ANSYS solid-only thermal model. Phase-change latent heat effects and liquid-phase convection are not modelled explicitly due to ANSYS Student licence limitations, as noted in Section 1.4. This is a conservative simplification, since the actual PCM thermal performance during phase transition would exceed that predicted by the solid-only model [12].

3.3.3 Thermal Management Systems Modelled

This thesis models five distinct simulation systems, labelled System A through System E, plus a Baseline representing the bare, unprotected module. Each system is designed to answer a specific and clearly defined thermal question about the $LiFePO_4$ battery module under Mongolian winter or summer conditions. The five systems fall into three functional groups.

Group 1 — Passive cold-resistance tests (Systems A and D): These systems contain no heater and no electrical input. The module starts at room temperature (+20°C) and is placed in a −40°C ambient environment. The question being asked is: how long does the module remain above 0°C before cooling to the point where safe charging and discharging are no longer possible? System A uses aerogel insulation as the passive barrier; System D uses a phase change material slab. An identical bare, uninsulated module simulation (the Baseline) is run alongside each of these systems under the same boundary conditions, enabling a direct comparison of the time at which the minimum cell temperature crosses 0°C.

Group 2 — Active heating tests (Systems B and C): These systems start with the module at −40°C and apply a heating source. The question is: how quickly can the heating source raise every part of the module above 0°C? System B uses an external PTC resistive heating plate. System C uses AC self-heating, in which an alternating current is passed through the cells themselves, generating heat internally and uniformly throughout the cell volume.

Group 3 — Combination and optimisation (System E): System E runs five sub-simulations combining elements from the four individual systems. Its objective is to identify the most effective and most energy-efficient combination of strategies. Critically, System E also introduces a summer overheating scenario, evaluating whether the aerogel insulation that protects the module in winter becomes a hazard when ambient temperatures are high and the cells are generating heat during discharge.

System A — Aerogel Insulation (Passive Cold-Resistance Baseline)

Physical configuration: The twelve-cell module is wrapped on all external faces with a 7.5 mm thick layer of aerogel blanket with thermal conductivity 0.016 W/(m·K), which is roughly five times better than conventional foam insulation [5]. In the ANSYS model, the aerogel is represented as a solid body surrounding the module on all six faces, with material properties as defined in Section 3.3.2. No heater, no PCM, and no electrical source is present.

Simulation question: How much longer does aerogel insulation allow the module to remain above 0°C compared to a completely uninsulated module, when both start at +20°C and are exposed to a −40°C ambient?

System B — External Heating Plate (PTC Resistive Heater)

Physical configuration: The heating plate is an aluminium block measuring 404.14 mm × 200.33 mm × 10 mm, with a concave pocket (352.14 mm × 146.33 mm × 6 mm deep) machined into the outer face. The plate sits flush against the large face of the module through a contact conductance boundary condition representing the physical 0.5 mm TIM layer. No aerogel and no PCM are present. The heater operates from the 12 V vehicle auxiliary electrical system, drawing 12.5 A for a total power of 150 W. This power is distributed evenly across the inner face of the heater plate contact area (0.08097 m^2), yielding a surface heat flux of 1,852 W/m^2, applied in ANSYS as a surface heat flux boundary condition.

Simulation question: Starting from a fully cold-soaked module at −40°C, how long does the 150 W external heating plate take to raise the minimum temperature anywhere inside the twelve cells to 0°C?

System C — AC Self-Heating (Internal Volumetric Heat Generation)

Physical configuration: An alternating current is passed through the battery pack without any other thermal management strategy. At −39°C, the internal resistance of a $LiFePO_4$ cell is approximately 25 mΩ [3]. An alternating RMS current of 50 A flowing through this resistance produces a dissipated power of $P = I^2 \times R = 50^2 \times 0.025 = 62.5$ W per cell. Across twelve cells, the total heat generation is 750 W, five times greater than the external heater in System B. The 62.5 W per cell is divided by the cell body volume (0.001146 m^3) to give a volumetric heat generation rate of 54,538 W/m^3,

applied as an Internal Heat Generation boundary condition to all twelve cell bodies in ANSYS Transient Thermal.

Simulation question: Starting from −40°C, how long does AC self-heating take to raise the minimum cell temperature above 0°C, and how uniform is the temperature distribution during warm-up?

System D — Phase Change Material Buffer (Passive Thermal Inertia)

Physical configuration: A 3 mm slab of RT35 phase change material is attached to the large face of the module opposite to where the heating plate sits in other systems. The slab dimensions are 404.14 mm × 200.33 mm × 3 mm. RT35 is a commercial paraffin-based PCM manufactured by Rubitherm GmbH, with a phase transition temperature centred near 35°C and a latent heat of approximately 160 kJ/kg [12]. No heater and no aerogel are included.

Important note: RT35 has a melting temperature of approximately 35°C, which is above the initial simulation temperature of +20°C. The PCM is therefore entirely in its solid phase at t = 0 and remains solid throughout the simulation window. No latent heat contribution is realised in the simulation. The effective thermal contribution of the PCM in this simulation is sensible heat only: $Q_{sensible}$ = 0.214 kg × 2,500 J/(kg·K) × 60 K ≈ 32.1 kJ, for cooling from +20°C to −40°C. The latent heat benefit (approximately 34.2 kJ) would additionally be available only if a prior high-rate discharge session had heated the cells above 35°C, melting the PCM before parking. This conditional scenario is not modelled; the System D result therefore represents a conservative lower bound on PCM performance.

Simulation question: How much longer does the PCM slab allow the module to remain above 0°C compared to a bare module, when both start at +20°C and are exposed to −40°C ambient? This question is structurally identical to the question in System A, allowing a direct comparison of aerogel versus PCM as passive cold-weather protection strategies.

System E — Combined Systems and Optimisation

System E deliberately combines elements from Systems A through D to determine which pairings produce the best thermal outcome per unit of energy consumed. System E also introduces a summer overheating scenario, which the individual systems do not address. This is important because a thermal management solution that protects the battery in winter must not trap excessive heat in summer, particularly if aerogel insulation is used. System E consists of five sub-simulations, as described in Table 4.

Table 4: System E sub-simulation configurations. E1 to E4 are cold-start tests; E5 is the summer overheating test.

Sub-simulation	Components and scenario
E1	External PTC heater + aerogel insulation. Cold start at −40°C.
E2	AC self-heating + aerogel insulation. Cold start at −40°C.
E3	External PTC heater + aerogel insulation + PCM slab. Cold start at −40°C.
E4	AC self-heating + aerogel insulation + PCM slab. Cold start at −40°C.
E5	Aerogel insulation only. Ambient +35°C, module initial temperature +20°C, internal heat generation 20,000 W/m³ (moderate highway driving).

Sub-simulations E1 and E2 pair an active heating strategy with aerogel insulation, to test whether retaining the internally generated heat within the aerogel envelope reduces warm-up time compared to the uninsulated Systems B and C. Sub-simulations E3 and E4 add the PCM slab to E1 and E2, respectively, to determine whether the additional thermal mass of the PCM further improves or hinders warm-up. Sub-simulation E5 tests the module with aerogel insulation only under a summer ambient of +35°C and an internal heat generation of 20,000 W/m^3, representing moderate highway driving. The maximum cell temperature at 60°C (the safe discharge temperature limit) is the pass/fail criterion for E5.

3.3.4 Boundary Conditions and Evaluation Metrics

Because each simulation system is designed to address a distinct research objective, the boundary conditions vary accordingly. These include the initial state of the module, the environmental conditions applied at its boundaries, and the duration of the simulation. This section systematically defines these parameters for each system and establishes the numerical metrics used to evaluate and compare their performance.

The following conditions apply to every simulation in this thesis unless the per-system description below explicitly states otherwise. A convection coefficient of h = 25 W/(m^2·K) is applied to all exposed outer surfaces. This value represents moderate

forced convection conditions within a battery enclosure, consistent with values used in module-level battery thermal finite element analyses in the published literature [3]. It is applied uniformly across all systems to ensure that differences in simulation results reflect differences in thermal management strategy rather than differences in assumed convective environments. Natural convection in still air produces h in the range of 5 to 10 W/(m^2·K); dedicated liquid or air cooling channels can exceed 50 W/(m^2·K). The selected value of 25 W/(m^2·K) is a standard mid-range assumption for this type of analysis.

Cell-to-cell thermal contact conductance of 6,000 W/(m^2·K) is applied to each pair of adjacent cell faces in all systems. This conductance is derived from the thermal conductivity and compressed thickness of the physical TIM pad that would be present between adjacent cells in a real assembly:

$$h_c = k / t = 3.0 \text{ W/(m·K)} / 0.0005 \text{ m} = 6{,}000 \text{ W/(m²·K)}$$

where k = 3.0 W/(m·K) is the bulk thermal conductivity of the silicone-based thermal interface pad [17] and t = 0.5 mm is the nominal compressed pad thickness. With eleven cell-to-cell interfaces in the 12S1P module, eleven contact pairs carry this conductance value in each system.

The boundary conditions for all six systems are summarised in Table 5.

Table 5: Boundary conditions applied to all six simulation systems. Heat retention systems start at +20°C; heat-up systems start at −40°C.

Boundary Condition	Baseline	System A	System B	System C	System D	System E
Test type	Heat retention	Heat retention	Heat-up	Heat-up	Heat retention	Combined
Initial temperature	+20°C	+20°C	−40°C	−40°C	+20°C	Variable
Ambient temperature	−40°C	−40°C	−40°C	−40°C	−40°C	−40°C / +35°C
Convection h	25 W/(m²·K)	25 W/(m²·K)	25 W/(m²·K)	25 W/(m²·K)	25 W/(m²·K)	25 W/(m²·K)
Surfaces with convection	All outer module faces	Outer aerogel faces	Module + heater outer faces	All outer module faces	PCM outer + other module faces	System-dependent

Boundary Condition	Baseline	System A	System B	System C	System D	System E
Heat source type	None	None	Heat flux on heater inner face	Internal heat gen. in cells	None	System-dependent
Heat source magnitude	—	—	1,852 W/m²	54,538 W/m³	—	System-dependent
Contact cond. (cell-cell)	6,000 W/(m²·K)	6,000 W/(m²·K)	6,000 W/(m²·K)	6,000 W/(m²·K)	6,000 W/(m²·K)	6,000 W/(m²·K)
Contact cond. (module-heater)	—	—	6,000 W/(m²·K)	—	—	If heater present
Contact cond. (module-PCM)	—	—	—	—	6,000 W/(m²·K)	If PCM present
Simulation end time	14,400 s	14,400 s	14,400 s	7,200 s	14,400 s	Up to 14,400 s

The per-system boundary conditions and primary evaluation metrics are as follows.

System A: Initial temperature +20°C applied uniformly to all module and aerogel bodies. Ambient temperature −40°C applied to all outer aerogel surfaces. Active heat source: none. The Baseline (bare, uninsulated module) is run under the same boundary conditions. Primary metric: $\Delta t_A = t_{insulated} - t_{bare}$, where $t_{insulated}$ is the time at which the minimum cell temperature crosses 0°C in the aerogel-insulated module and t_{bare} is the corresponding time in the Baseline. A larger Δt_A indicates more effective passive cold-weather protection. Secondary metric: initial rate of temperature drop in the first 600 s, and minimum, maximum, and mean cell temperatures at t = 1,800 s.

System B: Initial temperature −40°C applied uniformly to all module and heater plate bodies. Ambient temperature −40°C applied to all outer surfaces including the outer face of the heater plate. A surface heat flux of 1,852 W/m^2 is applied to the inner face of the heater plate, representing a total heater power of 150 W distributed over the contact area A = 0.40414 × 0.20033 = 0.08097 m^2:

$$q = P / A = 150\ W / 0.08097\ m^2 = 1{,}852\ W/m^2$$

An additional contact conductance of 6,000 W/(m^2·K) is applied between the heater plate inner face and the adjacent module face, representing the physical TIM pad. Primary metric: t_B, the time at which the minimum cell temperature first rises above 0°C from −40°C. If 0°C is not reached within 14,400 s, this is recorded as a failure finding.

Secondary metric: temperature non-uniformity $\Delta T = T_{max} - T_{min}$ across the twelve cells at the end of simulation.

System C: Initial temperature −40°C. Ambient temperature −40°C applied to all outer module faces. An Internal Heat Generation of 54,538 W/m^3 is applied uniformly to all twelve cell bodies:

$$q_{gen} = P_{cell} / V_{cell} = 62.5 \text{ W} / 0.001146 \text{ m}^3 = 54{,}538 \text{ W/m}^3$$

Primary metric: t_C, the time for the minimum cell temperature to rise above 0°C. The ratio t_B / t_C is used as a comparative heating rate metric. Secondary metric: temperature non-uniformity at t_C.

System D: Initial temperature +20°C applied to all module and PCM slab bodies (the PCM is in solid phase at this temperature). Ambient temperature −40°C. Active heat source: none. An additional contact conductance of 6,000 W/(m^2·K) is applied between the PCM slab face and the adjacent module face. The Baseline is run alongside System D using the same boundary conditions. Primary metric: $\Delta t_D = t_{withPCM} - t_{bare}$, compared directly with Δt_A from System A to evaluate aerogel versus PCM as passive strategies.

System E: Sub-simulations E1 through E4 begin at −40°C initial and −40°C ambient, with active heat sources corresponding to their component systems (E1 and E3 use a 1,852 W/m^2 heat flux on the heater plate; E2 and E4 use 54,538 W/m^3 internal heat generation). E3 and E4 additionally include the PCM slab with contact conductance 6,000 W/(m^2·K) between the PCM and the module. Sub-simulation E5 begins at +20°C initial and +35°C ambient, with internal heat generation of 20,000 W/m^3 in all twelve cell bodies. For E1 through E4, the primary metric is the time to reach 0°C minimum cell temperature. For E5, the primary metric is the maximum cell temperature at simulation end; a result at or below 60°C (maximum discharge temperature limit) constitutes a pass.

In addition to the per-system metrics, an overall efficiency ranking is produced in Chapter 4 for all systems involving active heating. Systems A and D are passive and consume no energy; their ranking is based on effectiveness (Δt) alone. Active systems are ranked by the metric:

$$\eta = \Delta T / (t_{warmup} \times P_{total})$$

where ΔT = 40°C (the temperature rises from −40°C to 0°C), t_{warmup} is the warm-up time in seconds, and P_{total} is the total electrical power input in watts. A higher η means more

temperature rise per watt of input power per second, indicating a more energy-efficient strategy.

The analysis settings applied consistently across all six Transient Thermal systems are listed in Table 6.

Table 6: Analysis settings applied to all six Transient Thermal systems.

Parameter	**Value**	**Unit**	**Notes**
Analysis type	Transient Thermal	-	All six systems
End time (Baseline, Systems A, D)	14,400	s	4 hours; heat retention test
End time (System B)	14,400	s	4 hours; heat-up test
End time (System C)	7,200	s	2 hours; heat-up test
End time (System E)	Up to 14,400	s	Varies by sub-simulation
Time step method	Auto Time Stepping	-	ANSYS default
Initial time step	1	s	-
Minimum time step	0.1	s	-
Maximum time step	60	s	All systems
Convergence criterion	Energy (default)	-	ANSYS default tolerance 1×10^{-3}
Solver type	Direct (Sparse)	-	ANSYS default thermal solver
Output: temperature	All nodes, all steps	-	-

Auto Time Stepping was enabled in all analyses, allowing ANSYS to reduce the time step automatically in the early stage of each simulation when temperature gradients are steepest, and to increase it as the solution approaches thermal equilibrium. Temperature results were recorded at all nodes for every converged time step. The primary output quantities extracted from each simulation are: the minimum cell body temperature (reflecting the coldest point in the module), the maximum cell body temperature (reflecting the hottest point), and the mean cell body temperature, all plotted against time.

4. Results

This chapter presents the results of all six transient thermal simulations. Sections 4.1 through 4.4 present the individual strategy results for Systems A, B, C, and D. Section 4.5 presents the System E combined and optimisation results. Section 4.6 provides a comparative summary and efficiency ranking across all systems. All temperature values are reported in degrees Celsius and all times are reported in seconds unless otherwise stated. The term "minimum cell temperature" refers to the lowest temperature recorded at any node within the twelve cell bodies at a given time step; it does not include the terminal bodies, aerogel, heater plate, or PCM slab.

4.1 System A: Aerogel Insulation

System A evaluates the passive thermal protection offered by 7.5 mm of aerogel insulation wrapped around all external faces of the module. The insulated module and an identical bare, uninsulated module (the Baseline) were both started at +20°C and exposed to a −40°C ambient for 14,400 s. The results are summarised in Table 7.

Table 7: Heat retention test results for the Baseline and System A. Time at which the minimum, maximum, and average cell temperatures cross 0°C.

Condition	Min. temp. crosses 0°C at (s)	Max. temp. crosses 0°C at (s)	Avg. temp. crosses 0°C at (s)
Baseline (bare module)	100	2,690	1,270
System A (aerogel insulated)	3,140	> 14,400	> 14,400
Δt (insulated − bare)	+3,040	-	-

In the bare Baseline module, the minimum cell temperature crossed 0°C after only 100 s (approximately 1.7 minutes). This confirms how rapidly an unprotected battery module loses heat to a −40°C environment. The maximum cell temperature in the Baseline (the warmest point, located in the centre of the stack) crossed 0°C at 2,690 s,

and the average crossed at 1,270 s. These three values show that the temperature distribution across the bare module is highly non-uniform from the earliest stages of cooling: the outermost cells, which are directly exposed to convection, cool far faster than the central cells.

With aerogel insulation, the minimum cell temperature remained above 0°C for 3,140 s (approximately 52.3 minutes). This represents an improvement of Δt_A = 3,140 − 100 = 3,040 s (approximately 50.7 minutes) relative to the Baseline. The factor of improvement in minimum-temperature protection time is 3,140 / 100 = 31.4. The maximum and average cell temperatures in the insulated module did not cross 0°C within the 14,400 s simulation window, meaning the central and average regions of the insulated module remained above the safe charging threshold for the entire 4-hour simulation period.

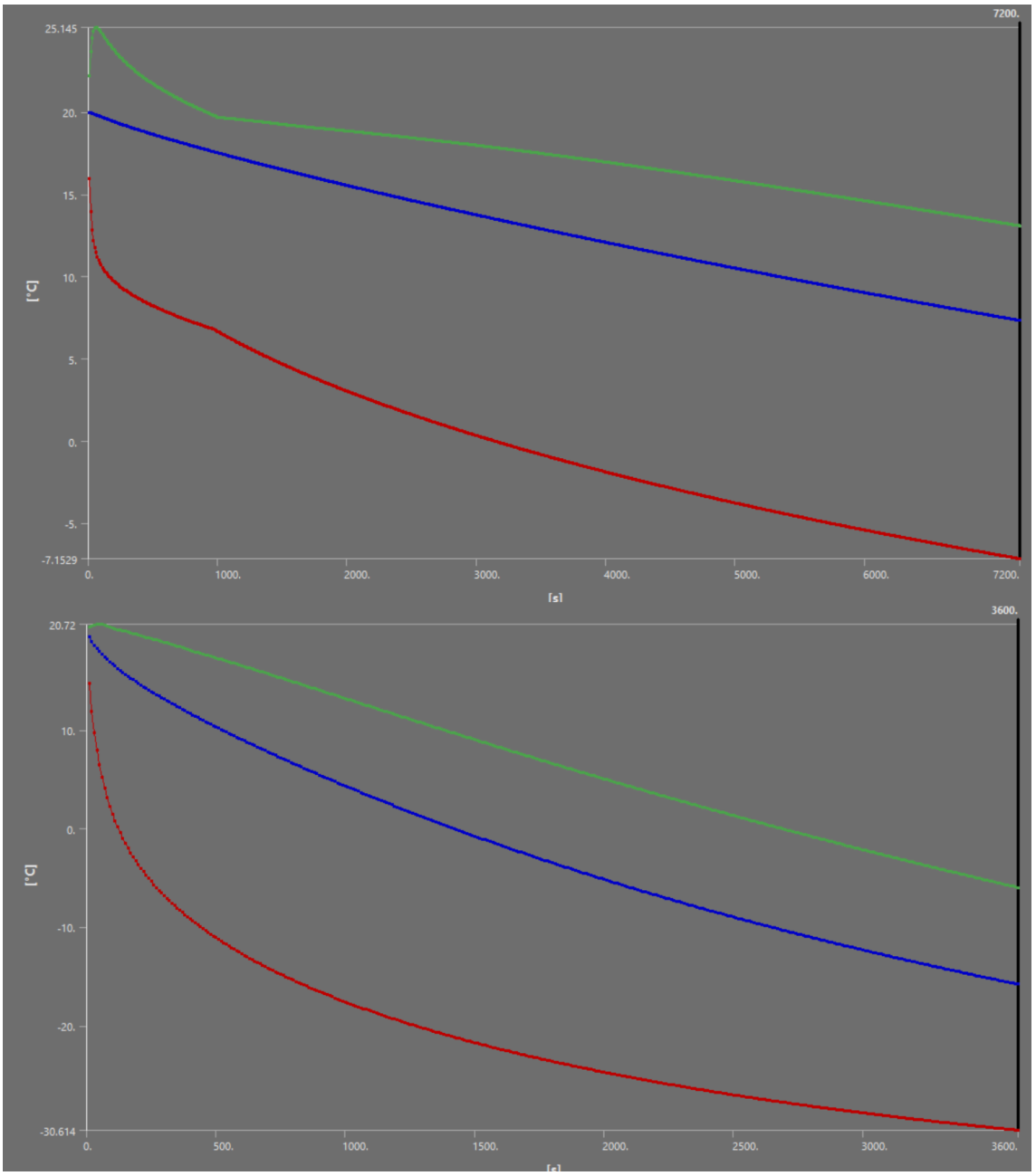


Fig.6: Minimum cell temperature versus time for System A and the Baseline. The aerogel extends the time above 0°C from 100 s to 3,140 s.

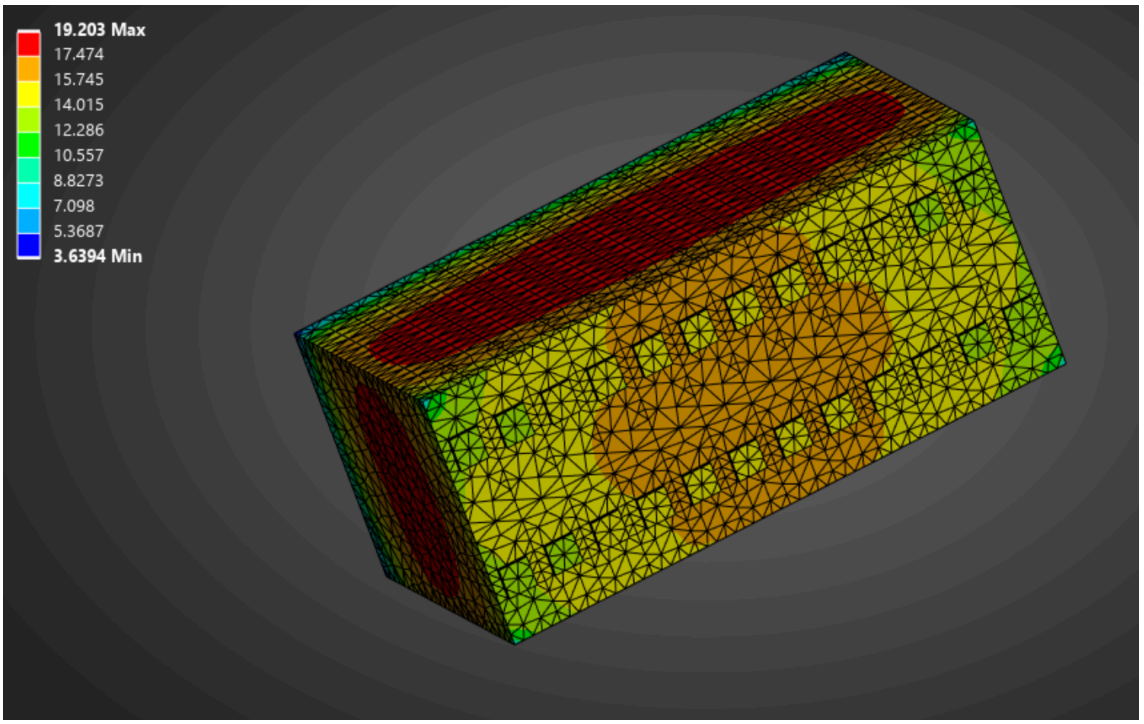


Fig.7: Temperature distribution across the aerogel-insulated module at t = 1,800 s. The aerogel envelope significantly reduces heat loss compared to the Baseline.

These results confirm that aerogel insulation is a highly effective passive cold-weather strategy for this module. A 7.5 mm aerogel layer provides over 50 minutes of additional protection at the minimum cell temperature and completely prevents the interior cells from crossing 0°C within 4 hours. However, the aerogel provides no active heat input: given sufficient time, the module will inevitably cool to the ambient temperature regardless of insulation quality.

4.2 System B: External PTC Resistive Heating

System B evaluates the ability of a 150 W external PTC heater plate to warm the module from −40°C to above 0°C (minimum cell temperature). The module and heater plate both begin at −40°C. The heater plate delivers a surface heat flux of 1,852 W/m^2 to the inner face, which is in thermal contact with one large face of the twelve-cell stack.

After the full 14,400 s (4-hour) simulation period, no part of the cell bodies reached 0°C. The minimum cell temperature at t = 14,400 s was −14°C. The maximum cell temperature (located at the cells immediately adjacent to the heater plate) reached approximately −2°C. This result unequivocally demonstrates that the 150 W external

PTC heater is insufficient, on its own, to pre-condition the module for safe charging or high-rate discharge from a cold start of −40°C within a practical timeframe.

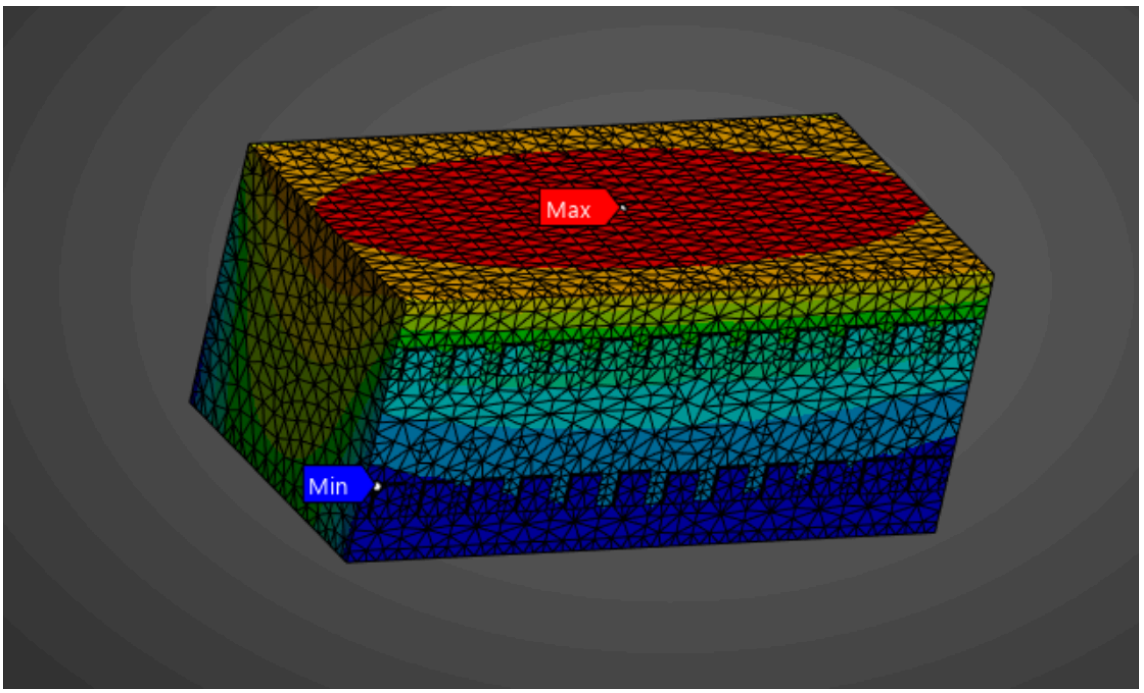


Fig.8: Temperature distribution across the module at the end of the System B simulation at t = 14,400 s. The cells adjacent to the heater plate are near −2°C while the far end of the stack remains near −14°C.

The physical explanation for this failure is twofold. First, the through-plane thermal conductivity of LFP cells is very low (k_z = 0.47 W/(m·K)), so heat applied at one face of the stack conducts very slowly to the cells on the far side. Second, the 150 W heat input must overcome convective heat loss from all outer module surfaces simultaneously exposed to the −40°C ambient. The module approaches an approximate thermal equilibrium in which the heat delivered by the heater is balanced by heat lost from the five non-heated faces. The thermal equilibrium minimum temperature of −14°C reflects this balance: the heater raises the temperature of the adjacent cells, but the far end of the stack cannot be sufficiently warmed within 4 hours by conduction alone at 150 W.

For context, the theoretical adiabatic minimum warm-up time (no heat loss, all 150 W going into cell thermal mass) is Q / P = 1,518,240 J / 150 W ≈ 10,122 s ≈ 2.8 hours. Since convective losses in the real simulation are significant, the actual warm-up requirement substantially exceeds this already large theoretical value, confirming that

150 W of surface heating is insufficient for this module size and temperature differential.

4.3 System C: Internal AC Self-Heating

System C evaluates internal AC self-heating, in which an alternating current passing through all twelve cells simultaneously generates 62.5 W per cell (750 W total) as internal Joule heat. This is represented in the simulation as a uniform volumetric heat generation of 54,538 W/m^3 applied to all cell bodies. The module begins at −40°C with no aerogel insulation.

The minimum cell temperature reached 0°C at t_C = 5,680 s (approximately 94.7 minutes). This represents a successful warm-up within a practically acceptable timeframe, in contrast to System B's failure. The energy consumed to reach 0°C is:

$$E_C = P_{total} \times t_C = 750\ W \times 5{,}680\ s = 4{,}260{,}000\ J = 1.183\ kWh$$

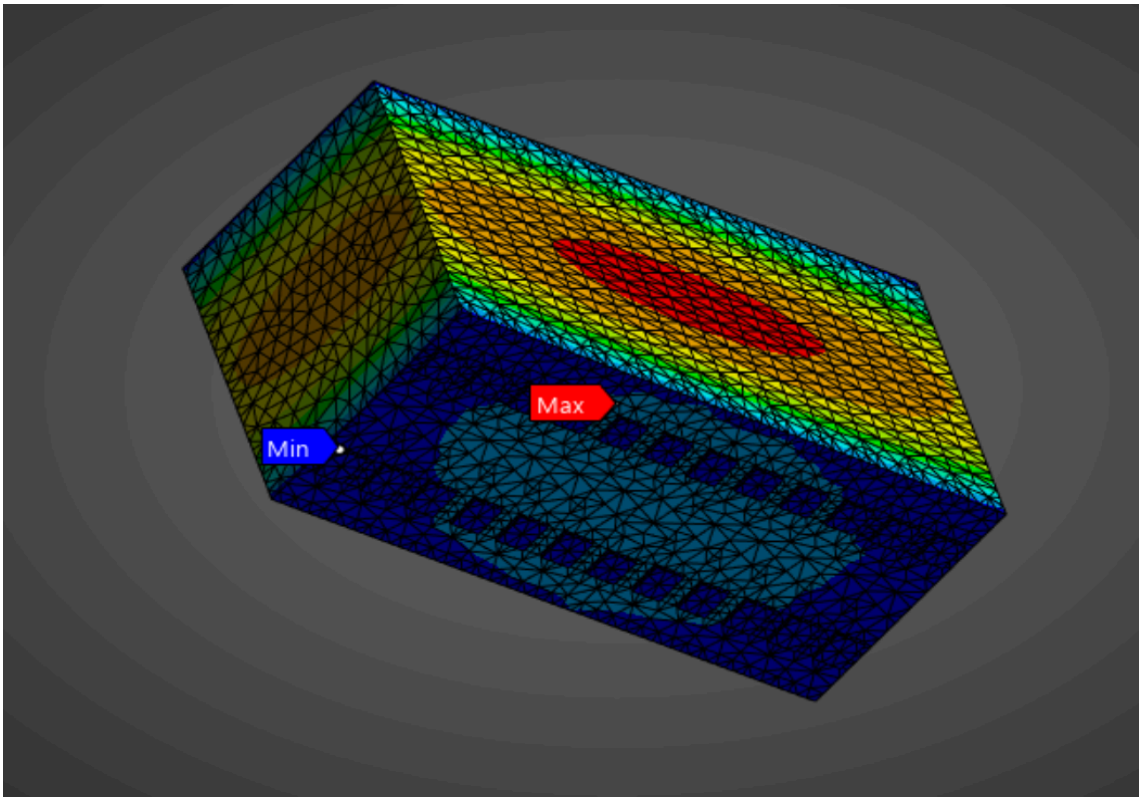


Fig.9: Temperature distribution at the moment the minimum cell temperature reaches 0°C in System C at t = 5,680 s. The temperature distribution is highly uniform, reflecting the even internal heat generation throughout all cell bodies.

A key observation is the high degree of temperature uniformity across the module at t_C. Because every cell generates heat internally and simultaneously, the temperature rise is distributed evenly. The temperature non-uniformity $\Delta T = T_{max} - T_{min}$ at t = 5,680 s is significantly lower than would be observed in System B at any equivalent moment. This uniformity is critical for module longevity: differential cell temperatures accelerate differential ageing and lead to cell-to-cell capacity mismatch over repeated charge-discharge cycles. System C is therefore superior to System B in both warm-up speed and temperature uniformity.

The ratio of System B end time to System C warm-up time is 14,400 / 5,680 ≈ 2.5, meaning AC self-heating completes warm-up in less than half the time System B ran without success, while also generating five times more total heat (750 W versus 150 W).

4.4 System D: Phase Change Material Buffer

System D evaluates the passive thermal protection offered by a 3 mm slab of RT35 PCM placed on the module face opposite to the heater location. The module and PCM slab both begin at +20°C in a −40°C ambient. An identical bare module (Baseline) is run under the same conditions. The results are summarised in Table 7 above, with the System D comparison shown in Table 8 below.

Table 8: Heat retention test results for System D (PCM slab) versus the Baseline. Small differences in Baseline values relative to Table 7 reflect independent simulation runs.

Condition	Min. temp. crosses 0°C at (s)	Max. temp. crosses 0°C at (s)	Avg. temp. crosses 0°C at (s)
Baseline (bare module)	95	2,670	1,270
System D (with PCM slab)	200	4,340	1,540
Δt (with PCM − bare)	+105	+1,670	+270

The bare module Baseline for System D shows a minimum temperature crossing of 95 s, slightly different from the 100 s obtained in the System A Baseline comparison. This minor difference (5 s, or 5%) arises from the independent ANSYS simulation runs and does not affect the conclusions; both Baseline values confirm that an unprotected module cools below 0°C in under two minutes.

With the PCM slab, the minimum cell temperature crossed 0°C at 200 s, compared to 95 s for the bare module. The additional protection provided by the PCM at the minimum temperature is therefore Δt_D = 200 − 95 = 105 s (approximately 1.75 minutes). This is a very small improvement compared to the 3,040 s provided by the aerogel in System A. The PCM is 3,040 / 105 ≈ 29 times less effective than aerogel at delaying the minimum cell temperature crossing.

The maximum cell temperature benefit of the PCM is more substantial: 4,340 s versus 2,670 s for the bare module, a difference of 1,670 s (approximately 27.8 minutes). The central cells in the stack benefit more from the additional thermal mass of the PCM slab because they are already partially shielded from convective cooling by the outer cells. However, the minimum temperature (the coldest cell, located at the end of the stack farthest from the PCM) sees almost no benefit because the PCM slab is in thermal contact with only one face of the module.

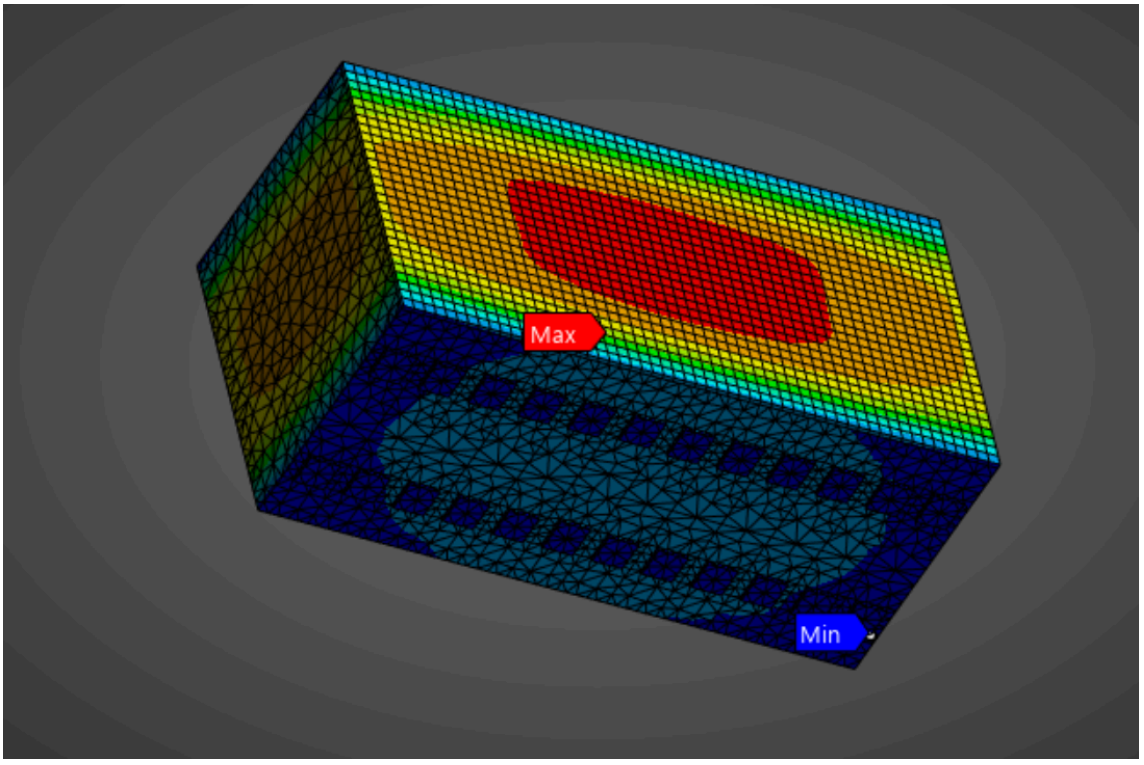


Fig.10: Temperature distribution across the module and PCM slab at t = 1,800 s (System D).

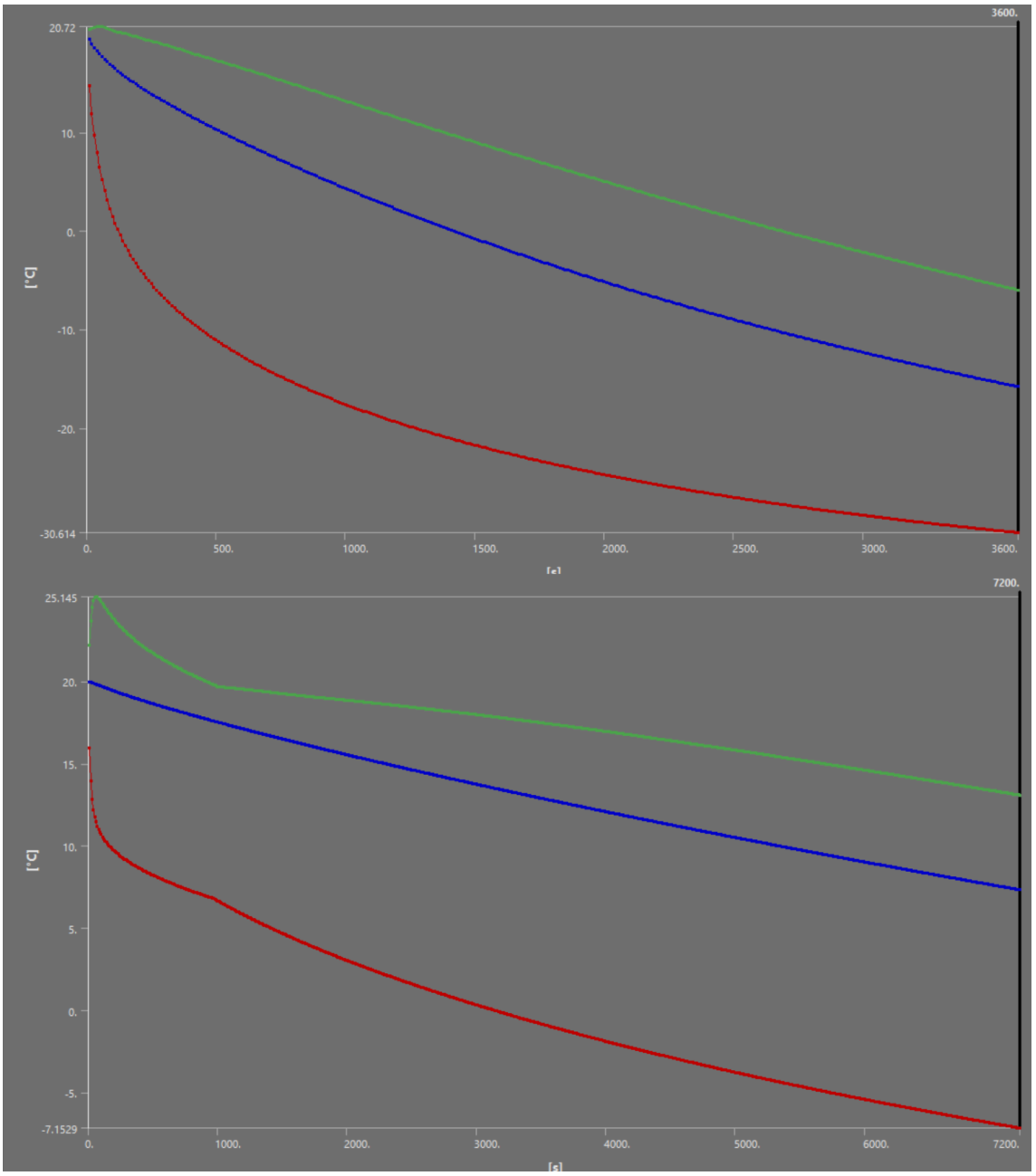


Fig.11: Minimum cell temperature versus time for System D and the Baseline. The PCM extends the minimum temperature protection by 105 s.

The reason for the PCM's limited effectiveness in this scenario is directly related to its material properties. RT35 has a melting point of approximately 35°C, which is above the initial simulation temperature of +20°C. The PCM enters the simulation already fully solidified, and no melting or solidification occurs during the cool-down from +20°C. The PCM therefore contributes only its sensible heat capacity as it cools from +20°C toward −40°C: approximately 32.1 kJ total. This is a very small heat reservoir compared to the

module's 12 × 2,636 g × 1,200 J/(kg·K) × 60 K ≈ 2,275 kJ of total thermal mass, explaining why the improvement is modest.

Comparing Systems A and D as passive strategies: aerogel (Δt_A = 3,040 s at minimum temperature) outperforms PCM (Δt_D = 105 s at minimum temperature) by a factor of approximately 29. Aerogel is clearly the superior passive cold-weather strategy for this module in Mongolian conditions.

4.5 System E: Combined Systems and Optimisation

4.5.1 Cold-Start Sub-Simulations E1 to E4

Sub-simulations E1 to E4 combine active heating strategies with passive insulation (and optionally PCM) to determine the most effective pairing. All begin at −40°C initial and −40°C ambient. Results are presented in Table 9.

Table 9: System E cold-start sub-simulation results. Energy consumed is calculated as P × t for active systems.

Sub-sim	Components	Time to 0°C min. (s)	Energy consumed (kWh)
E1	PTC heater + aerogel insulation	14,400 (exactly)	0.600
E2	AC self-heating + aerogel insulation	2,200	0.458
E3	PTC heater + aerogel + PCM slab	> 14,400 (FAIL)	> 0.600
E4	AC self-heating + aerogel + PCM slab	2,350	0.489

E1 (PTC heater + aerogel): The aerogel insulation dramatically changes the outcome of the PTC heater strategy compared to System B alone. In System B, the bare module exposed to −40°C convection lost heat from five surfaces simultaneously, and the 150 W heater could not overcome the heat loss. With aerogel wrapping all external surfaces, the only path for heat loss is through the aerogel envelope, whose very low thermal conductivity (0.016 W/(m·K)) severely restricts heat flow. As a result, the heater energy is retained within the module. The minimum cell temperature reached exactly 0°C at t = 14,400 s (precisely at the 4-hour simulation end), consuming E = 150 W × 14,400 s = 2,160,000 J = 0.600 kWh. While this is marginally successful (the minimum

temperature reaches the threshold just at the simulation boundary), it represents an extremely slow warm-up and high energy cost for a safety-critical pre-conditioning task.

E2 (AC self-heating + aerogel): This is the most effective sub-simulation. The combination of internally generated heat (750 W total, uniformly distributed through all cells) retained by the aerogel insulation produces a rapid warm-up. The minimum cell temperature reached 0°C at t = 2,200 s (approximately 36.7 minutes), consuming E = 750 W × 2,200 s = 1,650,000 J = 0.458 kWh. This is the shortest warm-up time of any active strategy tested and the lowest energy consumption among the active strategies that successfully reach 0°C. The aerogel reduces the warm-up time by (5,680 − 2,200) / 5,680 = 61.3% relative to System C alone, by preventing heat from escaping to the ambient during warm-up.

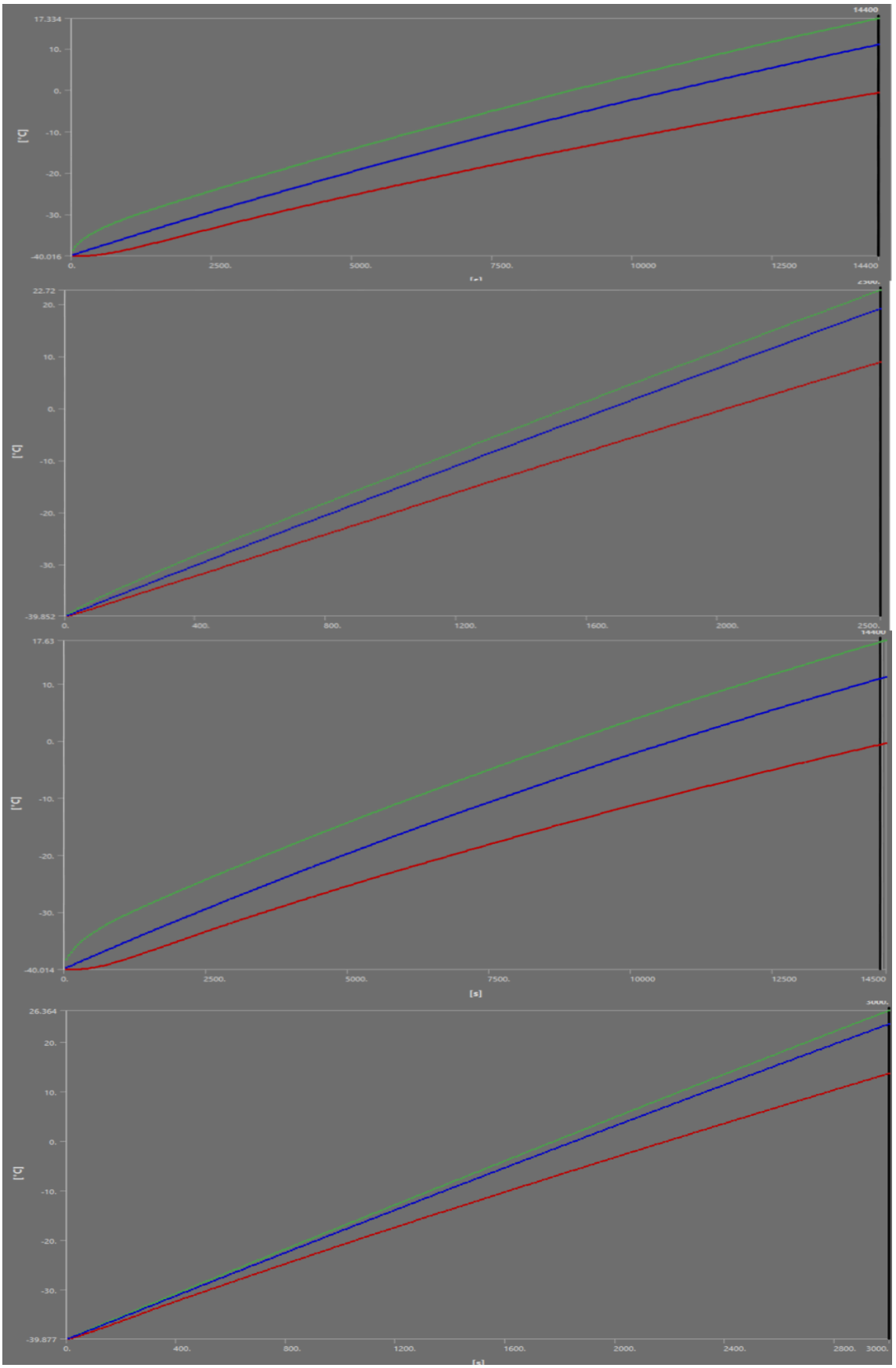


Fig.12: Minimum cell temperature versus time for System E sub-simulations E1 to E4. E2 achieves the fastest warm-up (2,200 s). E3 fails to reach 0°C within 14,400 s.

E3 (PTC heater + aerogel + PCM slab): Adding the PCM slab to E1 caused the system to fail. The minimum cell temperature did not reach 0°C within 14,400 s. The PCM slab, starting at −40°C alongside the module, acts as an additional cold thermal mass that absorbs heat from the heater before it can warm the cells. The 150 W heater must also heat the PCM from −40°C before any benefit can reach the cell that is farthest from the heater. The PCM slab therefore extends the warm-up time beyond the simulation window, making E3 strictly worse than E1. This is a critical result: it proves conclusively that PCM is detrimental in active cold-start scenarios where all components begin at sub-zero temperature.

E4 (AC self-heating + aerogel + PCM slab): Adding the PCM slab to E2 also extended the warm-up time, from 2,200 s (E2) to 2,350 s (E4), an increase of 150 s (6.8%). The energy consumed is E = 750 W × 2,350 s = 1,762,500 J = 0.489 kWh, compared to 0.458 kWh for E2. The PCM again acts as an additional heat sink at −40°C, absorbing some of the internally generated heat. However, the much larger heat generation of the AC strategy (750 W versus 150 W in E3) is sufficient to overcome this penalty and still achieve warm-up within the simulation window. The PCM is marginal but detrimental in E4.

These results from E3 and E4 together confirm the following principle: in a cold-start scenario where the module, PCM, and all other components begin at sub-zero temperature, adding a PCM slab with a 35°C melting point provides no latent heat benefit and acts purely as an additional cold thermal mass, increasing the energy and time required for warm-up. PCM is not a beneficial addition to any cold-start thermal management strategy for this module in Mongolian winter conditions.

4.5.2 Summer Overheating Sub-Simulation E5

Sub-simulation E5 evaluates the overheating risk when the aerogel-insulated module is subjected to warm-weather driving conditions. The module begins at +20°C (as if recently used or stored in a warm environment) with the aerogel insulation present. The ambient temperature is +35°C, representing peak summer conditions in Mongolia. An internal heat generation of 20,000 W/m^3 is applied to all twelve cell bodies, representing moderate highway driving. The total heat generation across all twelve cells is:

$$P_{total} = q_{gen} \times V_{cell} \times 12 = 20{,}000\ \text{W/m}^3 \times 0.001146\ \text{m}^3 \times 12 = 275\ \text{W}$$

The maximum cell temperature reached 60°C at t = 4,680 s (approximately 78 minutes). The maximum safe discharge temperature for this LFP cell is 60°C [15,16]. The

simulation therefore records a critical temperature exceedance at 78 minutes of moderate highway driving with aerogel insulation in +35°C summer ambient.

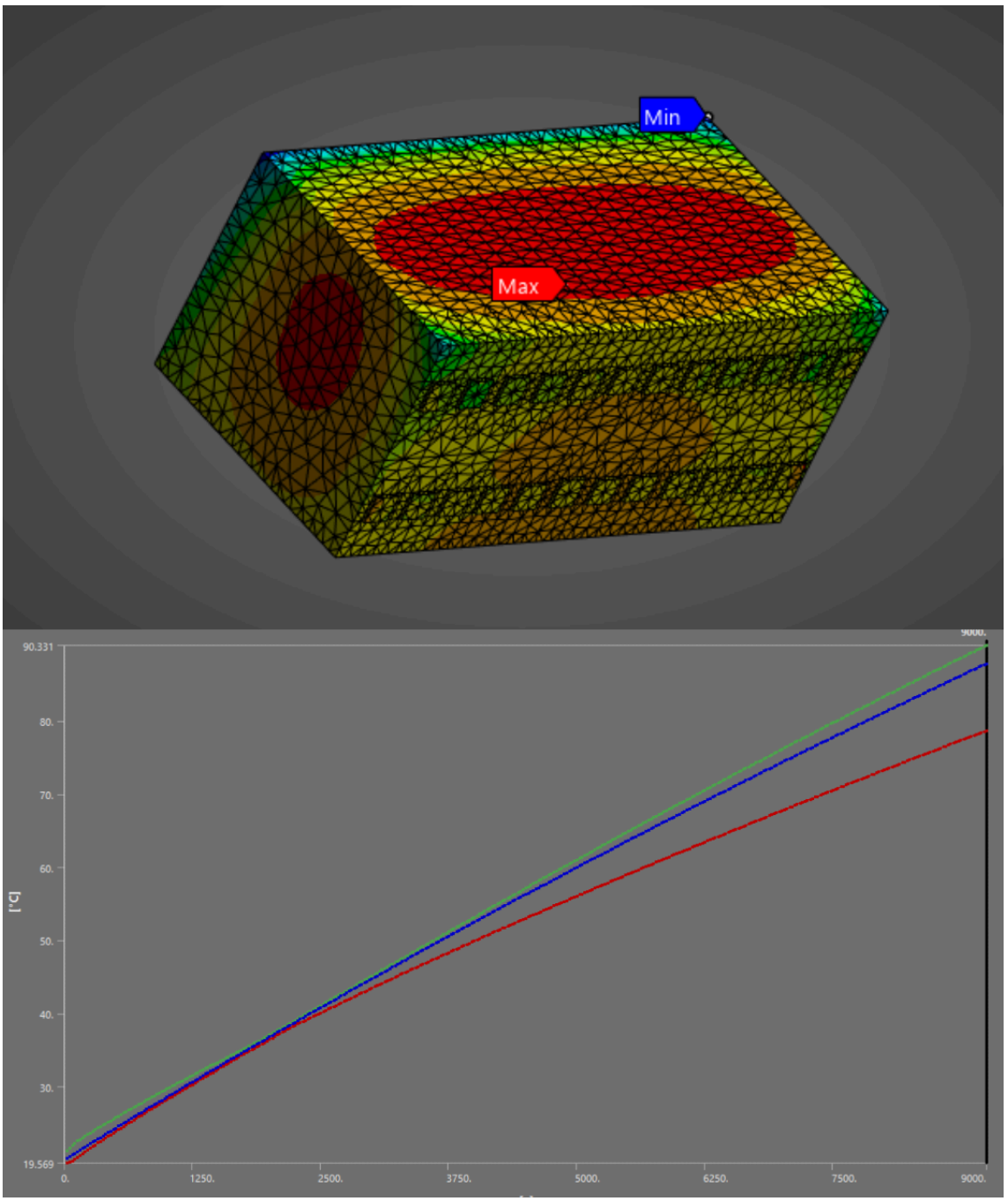


Fig.13: Temperature distribution in System E5 at the moment the maximum cell temperature reaches 60°C at t = 4,680 s. The aerogel envelope traps heat generated during moderate driving.

This result has a clear physical explanation. In winter, the aerogel reduces heat flow from the warm module to the cold ambient, which is the desired effect. In summer, it

identically reduces heat flow from the warm module to the warm (but cooler than the module) ambient. With 275 W of internal heat generation and effectively no path for heat to escape through the aerogel, the module temperature rises continuously. The ambient temperature of +35°C provides a small additional heat input at the start of the simulation (when the module is at +20°C, the ambient is warmer and adds heat), which accelerates the initial temperature rise further, explaining why the actual warm-up to 60°C (4,680 s) is faster than a purely adiabatic estimate would suggest.

This finding is a significant design constraint for any aerogel-based battery thermal management system deployed in Mongolia: the same insulation that is essential in winter creates a serious overheating hazard in summer under driving conditions. A practical solution must incorporate provisions for thermal management during warm-weather operation, such as thermally controlled ventilation panels in the aerogel enclosure or a parallel active cooling circuit.

4.6 Comparative Summary and Efficiency Ranking

Table 10: Comparative performance summary of all thermal management strategies. Energy consumed is calculated as $P_{total} \times t_{warmup}$ for active systems.

System	Strategy	Primary result	Energy consumed	Outcome
Baseline	Bare module	Min. at 0°C: 100 s	None (passive)	Reference
A	Aerogel insulation	Min. at 0°C: 3,140 s (+3,040 s)	None (passive)	Pass
B	PTC heater only (150 W)	Min. at 14,400 s: −14°C	0.60 kWh	FAIL
C	AC self-heating (750 W)	Min. at 0°C: 5,680 s	1.183 kWh	Pass
D	PCM slab only	Min. at 0°C: 200 s (+105 s)	None (passive)	Pass (marginal)
E1	PTC + aerogel	Min. at 0°C: 14,400 s	0.600 kWh	Pass (marginal)
E2	AC + aerogel	Min. at 0°C: 2,200 s	0.458 kWh	BEST
E3	PTC + aerogel + PCM	Min. at 14,400 s: < 0°C	> 0.600 kWh	FAIL

System	Strategy	Primary result	Energy consumed	Outcome
E4	AC + aerogel + PCM	Min. at 0°C: 2,350 s	0.489 kWh	Pass
E5	Aerogel, summer (+35°C, 20kW/m³)	Max. at 60°C: 4,680 s	—	Overheating risk

For all active systems that successfully reached 0°C, the efficiency metric $\eta = \Delta T / (t_{warmup} \times P_{total})$ is calculated, where $\Delta T = 40°C$ (the rise from −40°C to 0°C), warmup is the warm-up time in seconds, and P_{total} is the total electrical power input in watts. The results are ranked in Table 11.

Table 11: Efficiency ranking of active heating systems. $\eta = \Delta T / (t \times P)$. Systems B and E3 failed to reach 0°C and are not ranked.

Rank	System	Power (W)	$\eta = 40°C / (t \times P)$	Notes
1	E2	750	2.42×10^{-5} °C/(s·W)	AC self-heating + aerogel. Best efficiency.
2	E4	750	2.27×10^{-5} °C/(s·W)	AC + aerogel + PCM. Slightly penalised by PCM.
3	E1	150	1.85×10^{-5} °C/(s·W)	PTC + aerogel. Marginally successful.
4	C	750	0.939×10^{-5} °C/(s·W)	AC only. No insulation; large heat loss.
—	B	150	N/A (failed)	Never reached 0°C.
—	E3	150	N/A (failed)	PTC + aerogel + PCM. PCM made it worse.

The efficiency ranking reveals a consistent pattern: the combination of AC self-heating (large power input, uniform distribution) with aerogel insulation (preventing heat escape during warm-up) is the clear optimal strategy. E2 achieves the highest efficiency by a margin of 6.6% over E4, 31% over E1, and 158% over System C alone. System C (AC without insulation) ranks fourth despite having the same power as E2, because without aerogel, a significant fraction of the 750 W is lost to the −40°C ambient during

the 5,680 s warm-up period. System B and E3, both using the comparatively low-powered 150 W PTC heater, fail entirely or achieve only marginal success.

5. Discussion and Conclusions

5.1 Discussion

5.1.1 Effectiveness of Each Strategy

The simulation results demonstrate clearly differentiated performance among the four individual strategies and their combinations, providing a quantitative engineering basis for thermal management system design in Mongolian EV applications.

Aerogel insulation (System A): The 31-fold improvement in minimum-temperature protection time (from 100 s to 3,140 s) confirms that aerogel is an exceptionally effective passive cold-weather strategy for indoor-stored modules. The physical mechanism is straightforward: the very low thermal conductivity of the aerogel (0.016 W/(m·K), more than 29 times lower than the through-plane thermal conductivity of the LFP cell (k_z = 0.47 W/(m·K))) creates a powerful thermal barrier that slows heat exchange with the ambient. However, aerogel is a purely passive barrier and cannot prevent the battery from eventually cooling to the ambient temperature. A module stored outdoors without a heat source will ultimately equilibrate to −40°C regardless of insulation quality. Aerogel is therefore most effective as a complement to an active heating strategy, not as a standalone solution for vehicles that are parked outdoors overnight in Mongolian winter conditions.

External PTC heating (System B): System B's failure to reach 0°C after 4 hours of 150 W heating reveals a fundamental limitation of external surface heating for LFP modules in extreme cold. The through-plane thermal conductivity of LFP cells (k_z = 0.47 W/(m·K)) is so low that heat applied at one face of the 12-cell stack cannot efficiently reach the far end of the 398.64 mm-long stack within a practical timeframe. Additionally, the five non-heated module surfaces simultaneously lose heat to the −40°C ambient. The module approaches a thermal quasi-equilibrium at approximately −14°C (minimum) rather than continuing to warm. This result implies that significantly higher heater power, or a different heater placement (for example, on both large faces simultaneously), would be required for a PTC-only strategy to succeed in this scenario. System B alone is not recommended for Mongolian conditions.

AC self-heating (System C): System C's successful warm-up in 5,680 s with 1.183 kWh of energy demonstrates that internal heat generation is a viable pre-conditioning strategy. The key advantage over System B is not only the higher total power (750 W versus 150 W) but the spatial distribution of that power: every cell generates heat from within, so all cells warm simultaneously without the thermal resistance bottleneck of through-plane conduction. However, without insulation, a substantial fraction of the 750 W is continuously lost to the −40°C ambient throughout the 5,680 s warm-up period, increasing both time and energy cost. System C alone is effective but not energy-optimal.

Phase change material (System D): The very limited benefit of PCM in System D (+105 s at minimum temperature, compared to +3,040 s for aerogel) is consistent with the material physics. The RT35 PCM is already fully solidified at the +20°C start temperature. Its thermal contribution is limited to its sensible heat capacity as it cools: approximately 32.1 kJ across the full temperature range of +20°C to −40°C. This energy is a minor fraction of the total thermal mass of the module (approximately 2,275 kJ). Furthermore, the PCM slab is placed on only one face of the module (the face opposite the heater location), so the cells farthest from the PCM slab (which determine the minimum temperature) receive almost no benefit. System D provides marginal improvement over the Baseline and is not a viable standalone winter strategy for this module in Mongolian conditions.

System E — PCM is detrimental in cold-start scenarios: The E3 and E4 results provide unambiguous evidence that adding PCM to an active cold-start system makes performance worse. E3 failed entirely (PTC + aerogel + PCM versus E1's marginal success), and E4 took 150 s longer than E2 (AC + aerogel + PCM versus AC + aerogel). The mechanism is clear: when the entire system starts at −40°C, the PCM slab is a cold body that absorbs heat from the heater or from the cells. In a cold-start scenario, the PCM is purely a thermal load, not a thermal source. The higher-power AC strategy (E4) can overcome this penalty while the lower-power PTC strategy (E3) cannot. This finding is practically important: a designer who adds PCM to a battery thermal management system expecting improved cold-start performance will in fact make performance worse unless the PCM enters the session in a warmed or fully melted state.

System E — aerogel multiplies heating effectiveness: The comparison of E2 (2,200 s, 0.458 kWh) with System C (5,680 s, 1.183 kWh) illustrates the power of combining internal heat generation with external insulation. Aerogel reduces warm-up time by 61.3% and energy consumption by 61.3% (the same percentage, since power is fixed

and time is reduced proportionally). The aerogel does not generate heat; it simply prevents the heat already generated inside the cells from escaping to the cold ambient. This is the most efficient possible use of thermal insulation: it is applied during a period when the module is actively generating heat, so every joule saved from the ambient translates directly into faster warm-up.

5.1.2 Energy and Practical Considerations

From an energy perspective, E2 (AC self-heating + aerogel) consumes 0.458 kWh to pre-condition the module from −40°C to 0°C minimum. For a full battery pack containing multiple modules, the total pre-conditioning energy scales with the number of modules. For a representative small EV with a 40 kWh pack consisting of approximately 40 kWh / 3.84 kWh = 10.4 modules (approximately 11 modules), the total pre-conditioning energy would be approximately 11 × 0.458 = 5.0 kWh, corresponding to approximately 12.5% of pack capacity. This energy cost is significant but acceptable for a one-time pre-conditioning event before driving, and is partially offset by the reduced capacity loss that would otherwise occur if charging were attempted at −40°C.

From a practical installation perspective, the strategies differ significantly. Aerogel insulation is a passive, solid-state component that wraps the module exterior and requires no electrical connections. It adds minimal mass (the aerogel density is 150 kg/m^3, and a 7.5 mm layer around the module has a volume of approximately 0.00065 m^3 and a mass of approximately 0.1 kg) and is straightforward to integrate into the pack design. The PTC heater plate is a commercially available, well-understood component with self-regulating properties, but it draws power from the 12 V auxiliary electrical system and requires wiring and control logic. AC self-heating requires modifications to the battery management system to generate and control the alternating current signal; it does not require additional hardware but demands BMS capability that may not be present in all EV platforms. PCM integration is straightforward (the slab is placed against the module face) but is shown here to be counterproductive in the cold-start scenario and therefore is not recommended.

The summer overheating risk identified in E5 adds an important practical constraint. A module with aerogel insulation that exceeds 60°C in 78 minutes of moderate highway driving in +35°C summer ambient is a safety concern. In practice, this risk can be mitigated at the pack level by designing the aerogel enclosure with thermostatically controlled ventilation openings that allow airflow (and therefore convective cooling)

when the module temperature exceeds a threshold. The design and simulation of such a system is recommended as a priority for future work.

5.1.3 Limitations of the Study

The 32,000-node ANSYS Student licence constraint required a global mesh element size of 7.4 mm, which is sufficient for capturing module-level temperature gradients but cannot resolve sub-millimetre thermal phenomena within individual electrode layers. Finer meshes available under a full ANSYS licence would provide higher spatial resolution, particularly at the cell-to-cell contact regions.

The PCM is modelled as a solid with an effective specific heat capacity. This approach does not capture the isothermal latent heat absorption at 35°C, meaning the model underestimates PCM performance during actual phase transition. In a scenario where the module is first heated above 35°C (for example, by a prior driving session) and the PCM is melted before parking, the latent heat of 34.2 kJ would provide an additional thermal buffer not present in the solid-only model. The System D result therefore represents a conservative lower bound on PCM thermal performance for pre-melted modules.

The AC self-heating model uses a fixed heat generation rate of 54,538 W/m^3, derived from the internal resistance at −39°C. In reality, as the cell temperature rises, the internal resistance decreases (cells become more conductive), and for a fixed applied RMS current, the heat generation rate decreases. A more realistic model would include temperature-dependent internal resistance, which would reduce the heating rate as cells warm and may extend the warm-up time modestly.

The convection coefficient h = 25 $W/(m^2 \cdot K)$ is a fixed, uniform boundary condition. In practice, the convection coefficient inside a battery enclosure varies with vehicle speed, enclosure geometry, and the presence or absence of forced-air cooling. A lower h (representing more stagnant air inside the enclosure) would reduce heat loss in all systems and improve the performance of both passive and active strategies; a higher h would increase heat loss. The selected value is a standard assumption for this type of analysis and provides a reproducible basis for comparison.

This study is conducted at the module level. A complete battery pack contains multiple modules arranged within an enclosure, and the thermal interaction between adjacent modules, structural members, and the enclosure walls is not captured. The most important pack-level effect is that modules in the interior of a pack lose heat more

slowly than modules at the pack periphery, since they are partially shielded by adjacent modules. Pack-level simulations would be required to quantify this effect.

5.2 Conclusions

The following conclusions are drawn from the comparative transient thermal finite element analysis conducted in this thesis.

Conclusion 1: Aerogel insulation alone (System A) extends the minimum cell temperature protection time from 100 s (Baseline) to 3,140 s, a 31-fold improvement providing approximately 50 minutes of additional passive protection. Aerogel is the most effective standalone passive cold-weather strategy for this module, outperforming PCM by a factor of 29 at the minimum cell temperature.

Conclusion 2: External PTC heating alone (System B, 150 W) is insufficient for cold-start pre-conditioning in Mongolian conditions. After 4 hours at −40°C ambient, the minimum cell temperature reached only −14°C. The low through-plane thermal conductivity of LFP cells (k_z = 0.47 W/(m·K)) and the large convective heat loss from non-heated surfaces prevent this power level from achieving the necessary temperature rise within a practical timeframe.

Conclusion 3: Internal AC self-heating alone (System C, 750 W) can warm the module from −40°C to 0°C minimum in 5,680 s (94.7 minutes), consuming 1.183 kWh. Uniform internal heat generation provides significantly better temperature uniformity across the module than external surface heating, reducing cell-to-cell temperature differentials that contribute to differential ageing.

Conclusion 4: Phase change material alone (System D, RT35 PCM slab) provides minimal cold-weather benefit: only 105 s of additional minimum-temperature protection compared to the bare module, because the PCM is entirely solid at the +20°C start temperature and contributes only sensible heat. PCM is 29 times less effective than aerogel as a standalone passive cold-weather strategy for this module.

Conclusion 5: The combination of AC self-heating with aerogel insulation (System E2) is the optimal thermal management strategy, achieving 0°C minimum cell temperature in 2,200 s (36.7 minutes) with only 0.458 kWh of energy consumed. Adding aerogel reduces the warm-up time by 61.3% and energy consumption by 61.3% relative to AC

self-heating alone (System C), by retaining internally generated heat within the insulated module.

Conclusion 6: Phase change material is detrimental in active cold-start scenarios when all system components begin at −40°C. Adding PCM to the PTC + aerogel system (E3) caused complete failure; adding PCM to the AC + aerogel system (E4) extended warm-up time by 150 s. In both cases, the cold PCM mass acts as an additional heat sink, absorbing heat that would otherwise warm the cells.

Conclusion 7: Aerogel insulation creates a critical overheating risk during summer operation. With 20,000 W/m^3 of internal heat generation representing moderate highway driving in +35°C ambient, the aerogel-wrapped module exceeded the 60°C maximum discharge temperature in 4,680 s (78 minutes). Any aerogel-based thermal management system for Mongolian EVs must therefore incorporate provisions for warm-weather heat dissipation.

5.3 Recommendations for Future Work

Based on the findings of this study, the following directions are identified as priorities for future research.

Active cooling integration: The E5 overheating result confirms that aerogel-based modules require active thermal management capability for warm-weather operation. Future work should design and simulate a thermostatically controlled aerogel enclosure with ventilation openings, or a bypass cooling channel, that allows heat dissipation above a threshold temperature (for example, 40°C) while maintaining insulation below that threshold. Both passive ventilation (driven by buoyancy) and active forced-air cooling should be evaluated.

Full pack-level simulation: This study was conducted at the single-module level. A pack-level simulation would capture module-to-module thermal interactions, the effect of structural inter-module spacers, and the thermal behaviour of the pack enclosure. Of particular interest is whether interior modules in a multi-module pack achieve significantly longer heat retention times due to shielding by adjacent modules, which could inform pack layout optimization.

Temperature-dependent AC self-heating model: The fixed heat generation rate of 54,538 W/m^3 used in this study corresponds to the internal resistance at −39°C. A more realistic model would include the temperature-dependent internal resistance of LFP cells, which decreases as cell temperature rises. This would reduce the heat

generation rate dynamically during warm-up, potentially extending warm-up time and increasing energy consumption compared to the fixed-rate model. Accurate temperature-dependent impedance data at −40°C to 0°C would be required.

Enthalpy-method PCM modelling: The conservative solid-only PCM model used in this study does not capture the isothermal latent heat absorption at 35°C. A full ANSYS licence enabling the enthalpy-method phase-change model would provide more accurate results for scenarios in which the PCM enters the session in a pre-melted state (for example, following a prior driving session that heated the module above 35°C). This is the scenario in which PCM would provide its maximum benefit.

Aerogel thickness optimisation: The 7.5 mm aerogel thickness used in this study was selected as a practically representative value. A parametric study varying aerogel thickness from 2 mm to 20 mm would identify the optimal trade-off between cold-weather heat retention (which improves with thickness), warm-weather overheating risk (which worsens with thickness), and volumetric packaging constraints within the battery pack.

Experimental validation: The simulation results should be validated against bench experiments using a physical 12S1P module with a thermocouple array at key locations, subjected to the same boundary conditions as modelled. Validation of the System A (aerogel insulation) heat retention test and the System E2 (AC + aerogel) warm-up test would be the highest priority, as these represent the extremes of the performance range identified in this study

6. References

[1] Wang X, Chen Y, Chen Y. Online electric vehicle charging control with battery thermal management in cold environments [Preprint]. arXiv; 2026 [cited 2026 Apr]. Available from: https://arxiv.org/abs/2602.11561

[2] Tourist Information Center of Mongolia. Climate and weather of Mongolia [Internet]. Ulaanbaatar: Tourist Information Center of Mongolia; [cited 2026 Mar]. Available from: https://www.touristinfocenter.mn/en/cate4_more.aspx?ItemID=20

[3] Jaguemont J, Boulon L, Dube Y. A comprehensive review of lithium-ion batteries used in hybrid and electric vehicles at cold temperatures. Appl Energy. 2016;164:99–114. doi:10.1016/j.apenergy.2015.11.034

[4] Nilsson JF. Low temperature Li-ion battery ageing [Examensarbete 30 hp, UPTEC K14 022] [Internet]. Uppsala: Uppsala University; 2014 [cited 2026 Mar]. Available from: http://uu.diva-portal.org

[5] Aspen Aerogels Inc. Cryogel Z product data sheet: aerogel blanket for cold service applications [Internet]. Northborough (MA): Aspen Aerogels; 2020 [cited 2026 Mar 15]. Available from: https://www.aerogel.com/products-and-solutions/cryogel-z/

[6] Huamei World. What is the thermal conductivity of glass wool? [Internet]. [cited 2026 Mar]. Available from: https://www.huameiworld.com/news/what-is-thermal-conductivity-of-glass-wool.html

[7] Engineered Foam Products. EPS technical datasheet: expanded polystyrene [Internet]. [cited 2026 Mar]. Available from: https://www.engineeredfoamproducts.com/wp-content/uploads/2021/05/EFP-EPS-Technical-Datasheet-Expanded-Polystyrene.pdf

[8] Guo R, Li L, Sun Z, Xue X. An integrated thermal management system and control strategy for cabin and battery heating in range-extended electric vehicles under low-temperature conditions [Preprint]. SSRN; 2026 [cited 2026 Jan]. Available from: https://ssrn.com/

[9] Stuart TA, Hande A. HEV battery heating using AC currents. J Power Sources. 2004;129(2):368–78.

[10] Ji Y, Wang CY. Heating strategies for Li-ion batteries operated from subzero temperatures. Electrochim Acta. 2013;107:664–74.

[11] Wang CY, Zhang G, Ge S, Xu T, Ji Y, Yang XG, Leng Y. Lithium-ion battery structure that self-heats at low temperatures. Nature. 2016;529(7587):515–8.

[12] Rubitherm GmbH. RT35 phase change material — technical data sheet [Internet]. Berlin: Rubitherm GmbH; 2023 [cited 2026 Mar]. Available from: https://www.rubitherm.eu/en/index.php/productcategory/organische-pcm-rt

[13] Wikipedia contributors. Geography of Mongolia [Internet]. Wikimedia Foundation; [updated 2026; cited 2026 Mar]. Available from: https://en.wikipedia.org/wiki/Geography_of_Mongolia

[14] Mongolian Tour Guide. Mongolian capital Ulaanbaatar [Internet]. [cited 2026 Mar]. Available from: https://www.mongoliantour.guide/post/mongolian-capital-ulaanbaatar

[15] EVLithium. How does temperature affect lithium battery performance? [Internet]. [cited 2026 Apr 28]. Available from: https://www.evlithium.com/hot-lithium-battery/974.html

[16] EVLithium. CATL 100 Ah LiFePO4 prismatic cell specifications [Internet]. [cited 2026 Apr 28]. Available from: https://www.evlithium.com/catl-battery.html

[17] Henkel Electronic Materials LLC. Bergquist gap pad TGP 3000 thermal interface material data sheet [Internet]. Bloomington (MN): Henkel; [cited 2026 Apr 28]. Available from: https://www.henkel-adhesives.com/bergquist_gap_padtgp3000.html

7. Statutory Declaration

I hereby declare that this thesis, submitted in partial fulfilment of the requirements for the Bachelor of Engineering degree at the German-Mongolian Institute for Resources and Technology (GMIT), is my own original work. All sources consulted, including publications, data, and online resources, have been acknowledged and cited in accordance with the Vancouver citation style. This work has not been submitted for any other degree or qualification at this or any other institution.

Ulaanbaatar, 2026

Signature: _____

Bilguun Dagvasambuu